REPORT DOCUMENTATION PAGE

Form Approved
OMB No. 0704-0188

1. AGENCY USE ONLY (Leave blank)	2. REPORT DATE 23 February 1995	3. REPORT TYPE AND DATES COVERED Final, 1 Feb 92 – 31 Jan 95

4. TITLE AND SUBTITLE
Fundamental Investigations of Creep & Fatigue of Dispersion Strengthened Nb Alloys

5. FUNDING NUMBERS
G - F49620-92-J-0136

PE - 61102F
PR - 2306
TA - AS

6. AUTHOR(S)
Amyia K. Mukherjee and David M. Farkas

7. PERFORMING ORGANIZATION NAME(S) AND ADDRESS(ES)
Department of Chemical Engineering
and Materials Science
University of California
Davis, CA 95616

8. PERFORMING ORGANIZATION
AFOSR-TR-96
0079

9. SPONSORING/MONITORING AGENCY NAME(S) AND ADDRESS(ES)
Directorate of Aerospace and Materials Sciences
Air Force Office of Scientific Research
110 Duncan Ave, Suite B115
Bolling AFB, DC 20332-8080

AGENCY REPORT NUMBER

11. SUPPLEMENTARY NOTES

12a. DISTRIBUTION/AVAILABILITY STATEMENT

Unlimited, approved for public release.

12b. DISTRIBUTION CODE

13. ABSTRACT (Maximum 200 words)

During the three years of this program, the creep studies focused on a select precipitation strengthened alloy of niobium shown to posses superior creep resistance at stress levels normally targeted in design applications. The alloy selected was a carbide preipitation strengthened niobium-zirconium-alloy (Nb-1wt%Zr-0.1wt%C) commercially known as PWC-11. The carbide precipitations are produced in-situ during the thermomechanical processing of the material and have proven to be extremely stable at service temperature. Transmission electron microscopy was used to examine both the internal structure of the crept material as well as the size distribution of the carbide particles extracted from the metal matrix. X-ray diffraction analysis of the extracted carbide particles identified their chemical make-up necessary for characterizing their thermodynamic stability. A thermodynamic model was developed which supports the observed parameters of the carbide precipitates and thus is useful in predicting the high temperature mechanical properties of this and similar alloy systems.

14. SUBJECT TERMS
niobium, creep, coarsening

15. NUMBER OF PAGES
64

16. PRICE CODE

17. SECURITY CLASSIFICATION OF REPORT	18. SECURITY CLASSIFICATION OF THIS PAGE	19. SECURITY CLASSIFICATION OF ABSTRACT	20. LIMITATION OF ABSTRACT
Unclassified	Unclassified	Unclassified	Unlimited

NSN 7540-01-280-5500

DTIC QUALITY INSPECTED 1

Standard Form 298 (Rev. 2-89)
Prescribed by ANSI Std. Z39-18
298-102

19960321 080

GENERAL INSTRUCTIONS FOR COMPLETING SF 298

The Report Documentation Page (RDP) is used in announcing and cataloging reports. It is important that this information be consistent with the rest of the report, particularly the cover and title page. Instructions for filling in each block of the form follow. It is important to *stay within the lines* to meet *optical scanning requirements*.

Block 1. Agency Use Only *(Leave blank)*.

Block 2. Report Date. Full publication date including day, month, and year, if available (e.g. 1 Jan 88). Must cite at least the year.

Block 3. Type of Report and Dates Covered. State whether report is interim, final, etc. If applicable, enter inclusive report dates (e.g. 10 Jun 87 - 30 Jun 88).

Block 4. Title and Subtitle. A title is taken from the part of the report that provides the most meaningful and complete information. When a report is prepared in more than one volume, repeat the primary title, add volume number, and include subtitle for the specific volume. On classified documents enter the title classification in parentheses.

Block 5. Funding Numbers. To include contract and grant numbers; may include program element number(s), project number(s), task number(s), and work unit number(s). Use the following labels:

C	-	Contract	PR	-	Project
G	-	Grant	TA	-	Task
PE	-	Program Element	WU	-	Work Unit Accession No.

Block 6. Author(s). Name(s) of person(s) responsible for writing the report, performing the research, or credited with the content of the report. If editor or compiler, this should follow the name(s).

Block 7. Performing Organization Name(s) and Address(es). Self-explanatory.

Block 8. Performing Organization Report Number. Enter the unique alphanumeric report number(s) assigned by the organization performing the report.

Block 9. Sponsoring/Monitoring Agency Name(s) and Address(es). Self-explanatory.

Block 10. Sponsoring/Monitoring Agency Report Number. *(If known)*

Block 11. Supplementary Notes. Enter information not included elsewhere such as: Prepared in cooperation with...; Trans. of...; To be published in.... When a report is revised, include a statement whether the new report supersedes or supplements the older report.

Block 12a. Distribution/Availability Statement. Denotes public availability or limitations. Cite any availability to the public. Enter additional limitations or special markings in all capitals (e.g. NOFORN, REL, ITAR).

DOD - See DoDD 5230.24, "Distribution Statements on Technical Documents."
DOE - See authorities.
NASA - See Handbook NHB 2200.2.
NTIS - Leave blank.

Block 12b. Distribution Code.

DOD - Leave blank.
DOE - Enter DOE distribution categories from the Standard Distribution for Unclassified Scientific and Technical Reports.
NASA - Leave blank.
NTIS - Leave blank.

Block 13. Abstract. Include a brief *(Maximum 200 words)* factual summary of the most significant information contained in the report.

**Block 14.** Subject Terms. Keywords or phrases identifying major subjects in the report.

Block 15. Number of Pages. Enter the total number of pages.

Block 16. Price Code. Enter appropriate price code *(NTIS only)*.

Blocks 17. - 19. Security Classifications. Self-explanatory. Enter U.S. Security Classification in accordance with U.S. Security Regulations (i.e., UNCLASSIFIED). If form contains classified information, stamp classification on the top and bottom of the page.

Block 20. Limitation of Abstract. This block must be completed to assign a limitation to the abstract. Enter either UL (unlimited) or SAR (same as report). An entry in this block is necessary if the abstract is to be limited. If blank, the abstract is assumed to be unlimited.

DISCLAIMER NOTICE
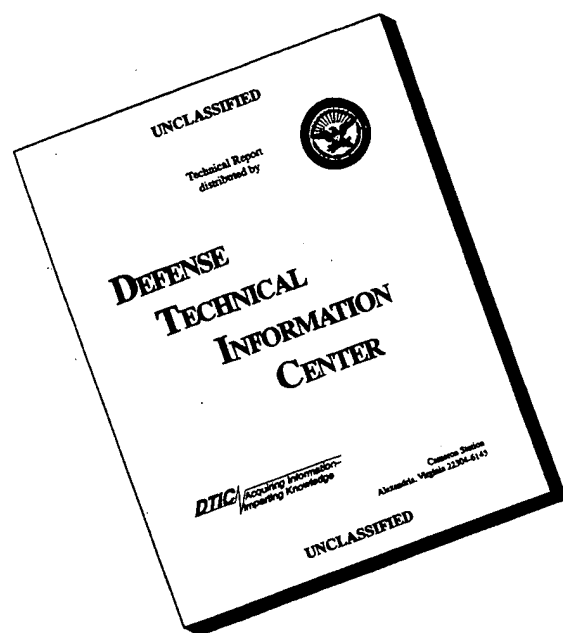
THIS DOCUMENT IS BEST
QUALITY AVAILABLE. THE
COPY FURNISHED TO DTIC
CONTAINED A SIGNIFICANT
NUMBER OF PAGES WHICH DO
NOT REPRODUCE LEGIBLY.

Final Technical Report

AFOSR GRANT NO. F49620-92-J-0136

Fundamental Investigations of Creep & Fatigue of Dispersion Strengthened Nb Alloys

Submitted to:

Dr. Charles Ward
AFOSR/NC
Building 410
Bolling Air Force Base
Washington D.C. 20332

Submitted by:

Professor Amiya. K. Mukherjee
and
David M. Farkas
Department of Chemical Engineering
and Materials Science
University of California
Davis, California 95616

February 23, 1995

CONTENTS

List of figures

1. Introduction

The focus of this research was to further the understanding of the fundamental mechanisms of high-temperature creep behavior in precipitation strengthened niobium alloys used for advanced aerospace structural applications. A key to this understanding lies in the role played by the particles in enhancing the materials creep resistance. Thus an investigation of the influence of parameters associated with the particles (such as particle size, spacing, volume fraction and high-temperature stability) was necessary. This project was a follow-on to a previous grant which examined the high-temperature mechanical behavior of pure and alloyed niobium as well as preliminary studies to enhance elevated temperature strength by creating particles via internal oxidation reactions with the matrix.

During the three years of this program, the creep studies focused on a select precipitation strengthened alloy of niobium shown to possess superior creep resistance at stress levels normally targeted in design applications. The alloy selected was a carbide precipitation strengthened niobium-zirconium alloy (Nb-1wt%Zr-0.1wt%C) commercially known as PWC-11 [Delgrosso, Carlson & Kaminski, (1967) and Titran, Moore & Grobstein, (1987)]. The carbide precipitations are produced "in-situ" during the thermomechanical processing of the material and have proven to be extremely stable at service temperature. Transmission electron microscopy (TEM) has been used to examine both the internal structure of the crept material as well as the size distribution of the carbide particles extracted from the metal matrix. X-ray diffraction (XRD) analysis of the extracted carbide particles identified their chemical make up necessary for characterizing their thermodynamic stability. A thermodynamic model was developed which supports the observed parameters of the carbide precipitations and thus is useful in predicting the high temperature mechanical properties of this and similar alloy systems.

2. Research Highlights

During the three years of our program, we have:

1. Refined the equipment, software and procedures used to perform both high-temperature monotonic creep tests and stress reductions tests up to 1450 K in vacuum.

2. Developed the techniques for the phase extraction of the carbide particles, TEM examination to determine their statistical size and spacing distribution, and XRD analysis of the precise particle chemistry needed for a thermodynamic model of their formation and stability.

3. Shown that the high-temperature creep behavior of carbide precipitation strengthened Nb-1wt%Zr-0.1wt%C is similar to that of the more simple Nb-1wt%Zr alloy at high stresses. The precipitation strengthened alloy only shows superior creep resistance at lower stress levels (which would be experienced in actual design applications). The presence of a so called "stress threshold for creep" is indicated.

4.   Shown that some (minor) particle growth occurs under creep conditions above 1400 K which results in a reduced creep resistance. Particle growth has not been seen in specimens crept under load at 1300 K for as long as 500 hrs.

5.   Shown that some unavoidable variation in material properties occurs during the thermomechanical processing of the alloy billet. This has implication in the commercial application of the material where uniformity of properties is needed to guarantee conformance to design requirements.

3.   Experimental Material and Procedure

3.1.   Materials

3.1.1   Composition and manufacturing

In the present study the carbide precipitation strengthened alloy Nb-1wt%Zr-0.1wt%C was used exclusively. The chemical composition of the material is listed in appendix A. The material, supplied by Martin Marietta Corporation (formerly General Electric Aerospace, SP-100 division), was processed by compacting powder, vacuum arc melting, canning and high-temperature extrusion at 1860 K, then swaged and rolled to sheet form for creep specimens. A two part final anneal was given to all creep specimens similar to that used in commercial application. Additionally, two specific final anneals were examined, one with 1 hr at 1877 K + 2 hrs at 1477 K to produce a target (large) grain size of 50 to 90 microns, the other with 1 hr at 1755 K + 2 hrs at 1477 K to produce a target (small) grain size of 20 to 27 microns. Further details of the manufacturing process and heat treatments are given in appendix A.

3.1.2   Material parameters

The matrix of the processed alloy, consisting of a dilute solid solution of zirconium in niobium, is of a body center cubic (bcc) crystal structure. In their final form, the carbide precipitates consist of a mixture of zirconium carbide (ZrC) and niobium carbide (ZrC) and have a face centered cubic (fcc) crystal structure. ZrC and NbC are completely soluble in one another thus form a solid solution which can vary in ZrC-to-NbC content. It will be shown that the zirconium to niobium ratio in the mixed carbide precipitate is a direct function of the heat treatment temperature. The difference in structure of the fcc carbide precipitates from the bcc niobium-zirconium alloy matrix affects the coherency of the particles with the matrix. The end result is that the particles are incoherent with the matrix and as such have some significant implications in the alloy's creep behavior and particle growth discussed later. The following tables list some of the significant material properties of the Nb-1wt%Zr-0.1wt%C alloy:

2

Table 1. Material properties of Nb-1wt%Zr-0.1wt%C matrix

Crystal structure	bcc
Density	8.5 g/cm^3
Melting temperature	2741 K
Burger's vector	0.286 nm
Modulus of elasticity (1300 K)	100 GPA
Activation energy (for creep)	400 - 450 kJ/mole

Table 2. Material properties of mixed carbide (ZrC + NbC) particles (as-received)

Crystal structure	fcc
Density	6.8 g/cm^3
Volume fraction	0.019
Mean particle diameter	0.16 μm
Lattice parameter	0.461 nm
ZrC to NbC ratio	1.66

3.2   Creep Testing

3.2.1   Sample preparation

Tensile specimens of Nb-1wt%Zr-0.1wt%C were provided with the two-part final anneal courtesy of Martin Marietta Corporation (formerly General Electric Aerospace, SP-100 division), San Jose, California. All creep specimens were electro-discharge machined parallel to the rolling direction. Prior to testing, all specimens were wrapped in niobium foil to preclude oxidation due to residual oxygen in the vacuum retort during the high temperature creep test. (Typically, a vacuum of less than 2 x 10^{-6} torr was maintained in the retort during creep testing.) Figure 1 shows a typical creep test specimen.

The actual measured grain sizes resulting from the final anneal heat treatment were:

Annealing temperature	Target grain size	Measured grain size
1 hr 1877 K + 2 hr 1477 K	50 - 90 microns	50 - 350 microns
1 hr 1755 K + 2 hr 1477 K	22 - 27 microns	10 - 40 microns

3.2.2   Test equipment

All creep testing was performed using a high-temperature vacuum furnace constant stress creep tester purchased from Applied Test Systems (ATS) with funding obtained from a previous AFOSR equipment grant. The complete test apparatus is shown in Fig. 2. Throughout the duration of this test program, we have continued to upgrade and improve the test techniques and

apparatus, especially the data acquisition interface and software. The more important upgrades are discussed in the following:

1. Installation of an industry standard high-speed digital voltmeter with associated IEEE-488 interface to a 80286 microprocessor based computer for data acquisition. This system allowed for different "mode" selections necessary for the faster data acquisition rates employed during transient stress change tests. An overall accuracy of strain measurement of 2×10^{-7} was achieved.

2. Rebuilding of the creep tester's extensiometer due to deterioration resulting from the internal oxidation experiments performed under the previous research grant.

3. Installation of a mullite ceramic retort to allow higher temperature creep testing (up to 1450 K).

4. Modification of the creep apparatus high-temperature furnace to enhance life of the Kanthal Super "33" heating elements. This modification was performed after an "in-house" review identified the faulty connection design of the factory arrangement. No failures have occurred in over 2000 hours of furnace operation following this modification saving not only replacement cost dollars but testing down time. This improvement was communicated back to the manufacturer (Applied Test Systems, Inc., Butler PA) for inclusion in future designs.

5. Installation of data acquisition and monitoring of the turbomolecular vacuum pumping system (running current, frequency and vacuum level). This provided real time information on performance trends of the vacuum pump which eventually identified the requirement to replace the pump. The turbomolecular pump was replaced with an unused oil diffusion pump cannibalized from previous research equipment.

3.2.3 Test methods

Two different test modes were employed during creep testing depending on the desired data acquisition rate and test parameters desired:

Normal mode - Used during monotonic creep testing to obtain strain (from measured elongation), applied stress (from measured load and cross-sectional area derived from elongation), temperature (measured at three points near the specimen), and strain rate (derived from computed strain and time). Acquisition rate was selectable based on time (2, 10, 60 sec or 10 min) or strain. Real time graphical representation of data (stress, strain, rate, temperature) was available to the researcher.

Fast mode - Used during stress cycling test. This mode recorded select parameters at a higher rate (10 data sets per second of stress, strain, and time). A "reduced strain rate" could easily be measured following stress changes which allowed accurate determination of the internal dislocation back stress discussed below.

3.3 Characterization

3.3.1 Transmission electron microscopy (TEM)

Sample preparation for TEM employed the standard methods described as follows. Initial mechanical thinning was performed on specimens to approximately 100 to 150 μm using up to 600 grit silicon carbide paper. Final electropolish (jet thinning) to perforation was then performed using an electrolyte consisting of 5% H_2SO_4, 2% HF, and 93% methanol. A voltage setting of 20V and an electrolyte temperature of -20 C allowed perforation in approximately 3 minutes. A final rinse in ethanol was made prior to storage for viewing.

TEM examination objectives included the determination of:
i.   Particle size.
ii.   Volume fraction of particles.
iii. Particle spacing.
iv.   Dislocation structures of deformed material (presence of subgrains, dislocation-particle attraction).
v.   Particle-matrix interface (degree of coherency).

The majority of the TEM examinations were performed on a Philips EM-400 or a Philips CM-12 operated at 120 kV. Additionally, several crept specimens were examined using the Kratos-1500 at the National Center for Electron Microscopy (NCEM) at Berkeley. The higher voltage (1.5 MeV) allowed greater specimen penetration and thicker regions to be examined for the microstructural features expected as a result of creep.

3.3.2 Phase extraction and particle analysis

A chemical phase extraction technique was used to remove the carbide precipitates from the niobium matrix to allow analysis of Nb and Zr content, crystal structure, lattice parameters and volume fraction. A solution of 900 ml methanol, 100 ml bromine, and 10 g of tartaric acid was used to dissolve the niobium matrix. Samples of the alloy were wrapped with a platinum wire catalyst, placed in the extraction solution, and ultrasonically agitated twice daily until the bulk matrix was fully dissolved. Typically 3 to 5 days were required to dissolve the niobium matrix. The solution was then centrifuged and decanted to remove the particles. Several dilutions and methanol washings were necessary to remove traces of the bromine. The methanol-carbide suspension was then evaporated on a "zero-background" plate for x-ray analysis or on an appropriate specimen holder for particle size measurement via TEM. The centrifuging technique was favored over filtering to improve the minimum particle size captured. Particle sizes as small as 40 nm were measured.

X-ray spectrums (counts per second versus two-theta/d-spacing) were obtained for the extracted particles using a SCINTAG model XDS-2000 X-ray diffractometer with Cu Kα radiation. The d-spacings from the highest three peaks were used in calculating the particle lattice parameter and for comparison with JCPDS 1978 standards for the listed carbides of niobium and zirconium (ZrC, NbC, Nb_2C and Nb_6C_5).

5

In order to determine the mean particle radius, the extracted particles were suspended in methanol, ultrasonically agitated for several minutes to disperse any agglomerations and dispensed on a formvar-coated 100 micron mesh copper grid for TEM analysis. The resulting micrographs were enlarged and individual particles were measured (to the nearest 1 mm). The measurement resolution was matched with the print magnification to assure the optimum "bin" size for the distribution function. (1 mm on print corresponded to approximately 0.01 μm actual size at the magnification used.) The distribution of particle sizes was then analyzed using a spread sheet program to determine the mean particle radius, and means of the radii squared and cubed.

4. Results and Discussion

4.1 Monotonic creep tests & approach to threshold stress

The creep behavior observed at each stress level was typically of the normal type, ie., an instantaneous strain jump followed by decreasing strain rate with time (primary creep) followed by an extended period of constant strain rate creep (secondary creep). Such behavior is typical for both pure metals and many class II creep alloys. The steady state strain rate at each stress level is plotted in Fig. 3 and compared to the steady state (or minimum) strain rates for pure Nb and Nb-1wt%Zr alloy [Davidson, Biberger and Mukherjee, (1992)].

The steady state creep rate can be described by the phenomenological relation:

$$\dot{\epsilon}_{ss} = A \sigma^n \exp\left(\frac{Q_c}{RT}\right) \tag{1}$$

where A is a constant, σ is the applied stress, n the stress sensitivity exponent, Q_c the activation energy for creep, R the gas constant and T the absolute temperature. The slope of the plot of log of steady state creep rate vs. log stress corresponds to n. In the present analysis for Nb-1wt%Zr-0.1wt%C, the slope n ≈ 6.3 indicating a rate controlling mechanism similar to that of pure Nb and the Nb-1wt%Zr alloy. Previous analysis had shown that for the Nb-1wt%Zr alloy, the stress level was high enough to allow dislocations to break away from solute atom drag, thus explaining why the solid solution strengthened alloy displayed class II creep behavior [Davidson, et.al.]. The departure from the straight line slope at high stress levels for the pure Nb and Nb-1wt%Zr alloy is attributed to power law breakdown [Areili and Mukherjee, (1981)].

In the stress range of 70 to 100 MPa, the creep rate of Nb-1wt%Zr-0.1wt%C is similar to that of the Nb-1wt%Zr alloy. Clearly in this stress range, the carbide particles offer little benefit to the alloy's creep strength. This is expected since at stress levels greater than the Orowan stress for dislocation-particle bypass (calculated herein), the precipitates offer no resistance to dislocation motion. The slight reduction in creep strength observed in comparing Nb-1wt%Zr-0.1wt%C with Nb-1wt%Zr is attributed to the lower Zr content remaining in solution, thus providing less solid solution strengthening.

6

The present study concentrated on the creep behavior at low stress levels. As can be seen in Fig. 3, strain rates lower than what is predicted by equation (1) for Nb-1wt%Zr-0.1wt% C are present at low stress levels (below about 20 MPa). This is a classic effect of the presence of a stress threshold, below which negligible creep occurs (by this mechanism). Again it must be emphasized that the accuracy of measurement of such low strain rates must be taken with caution, however the measured strain rate at 16 MPa is at least one order of magnitude *lower* than predicted by equation (1), clearly pointing to the presence of at least a pseudo-threshold.

Since NbC and ZrC display complete solid solubility for all composition ranges, Vegard's relation was be exploited to determine the composition based on measurement of the particle's lattice parameter [Norton and Morwey, (1949)]. For NbC-ZrC system, a slight negative deviation from linearity is present in the lattice parameter-composition curve, however in the present analysis a linear relation was assumed in determining composition. Since carbon forms non-stoichiometric carbides with both Nb and Zr, a lattice parameter range also introduced a slight error in composition calculation [Smith, Carlson & De Avillez, (1987)].

Figure 4 shows the X-ray spectrum from the extracted carbide particles of the as-received material. As can be seen, the intensity peaks of the particles lie between the intensity peaks for ZrC and NbC indicating a mixture of the two is present. The carbide mixture is typically given as (Nb,Zr)C and is of fcc structure [Grobstein and Titran, (1986)]. An average composition ratio of 62.5% ZrC to 37.5% NbC was determined from the first 3 intensity peaks of the X-ray spectrum. This chemical make up was used to calculate the volume fraction of particles present in the matrix. In this case volume fraction f was determined to be 0.019.

4.1.1 Particle size distribution and mean particle spacing

Figure 5 shows a TEM micrograph of the extracted (Nb,Zr)C particles from a sample of the alloy prior to creep testing. Note that for the most part, the particles are facetted and have a marked range of sizes. The particle size measurement was made on the longest dimension observed for a given particle. Figure 6 shows the size distribution histogram along with the mean of the distributions calculated from the size sampling made. These mean values and the volume fraction determined above were used to calculate the Orowan stress for dislocation particle bypass.

4.1.2 Calculation of Orowan stress based on average interparticle spacing

In order to determine if such an observed effect at low stress levels is theoretically valid, a calculation was made of the Orowan stress for dislocation particle bypass. Threshold stresses in particle-strengthened metals typically are calculated as a fraction of the Orowan stress [Cadek, (1988)], thus the first step in validating the existence of a threshold stress is to calculate the Orowan stress. (At applied stresses greater than the Orowan stress, dislocations will simply bypass the particles and overcome any stress threshold.) Additionally, since a spectrum of particle sizes was observed, a statistical analysis of the size distribution must be included to accurately determine the pinning length used in the Orowan equation. In this case the mean surface-to-surface interparticle spacing was used to estimate the Orowan stress from:

$$\tau_{OB} = \alpha \frac{Gb}{\overline{\lambda}} \qquad (2)$$

where α is a constant = 0.84 which relates to the strength of the particle-dislocation interaction, G is the shear modulus, and b is the Burger's vector. The mean value of particle radius; $\overline{r}$, the mean of the square of the radii; $\overline{r}^2$ and the mean of the cube of the radii; $\overline{r}^3$ were determined from the particle distribution histogram in Fig. 5 and used to calculate the mean interparticle spacing $\overline{\lambda}$ from [Yeh, et. al., (1990)]:

$$\overline{\lambda} = 1.25 \sqrt{\frac{2\pi}{3f} \frac{\overline{r}^3}{\overline{r}} - \frac{\pi}{2} \frac{\overline{r}^2}{\overline{r}}} \qquad (3)$$

The first term represents the mean center-to-center interparticle spacing in a distribution of randomly sized particles while the second term accounts for the particle's position on dislocation glide plane. A complete derivation of the statistical distribution of particle size and spacing is included in Appendix B for completeness. The volume fraction f was calculated from the chemical analysis of the alloy. Table 3 summarizes the parameters used to calculate the Orowan stress for dislocation particle bypass.

Table 3. Summary of parameters used to calculate Orowan Stress

Mean particle radius $\overline{r}$	0.079 μm
Particle volume fraction f	0.019
Average interparticle spacing $\overline{\lambda}$	1.081 μm
Shear modulus G	38.5 GPa
Niobium Burger's vector **b**	0.286 nm
Calculated Orowan (shear) stress for particle bypass	8.5 MPa

4.1.3   Threshold stress calculation

Threshold stresses in particle-strengthened materials arise from several potential mechanisms [Cadek, (1988)]. These include:

i.   Orowan bowing,
ii.   Particle shearing, and
iii.   Dislocation climb and particle bypass.

8

The first two are athermal meaning they do not require high temperature to operate. Orowan bowing in itself introduces a stress threshold and its calculation is treated herein. Particle shearing becomes more prominent with coherent or semi-coherent particles whose shear modulus does not differ greatly from that of the matrix. Particle shearing has not been observed in crept specimens of this alloy. The different crystal structures of the particles (fcc) compared to the matrix (bcc) favor incoherent interfaces and preclude particle shearing as an operative mechanism.

Dislocation climb over particles requires diffusional mass transport and is typically slower than Orowan bowing or particle shearing. Thus if Orowan bowing or particle shear are possible, they will dominate the observed creep behavior. Only when these two mechanisms do not occur (ie., at low stress levels and high temperatures) will dislocation climb operate and be rate controlling.

All models of threshold stress determination predict the threshold to be a fraction of the Orowan stress according to:

$$\tau_{th} = K\tau_{Orowan} \qquad (4)$$

where K is a constant (typically < 1) whose value depends on the particular model employed. For example, for local climb or particle detachment threshold models, K = 0.36 while for general climb models K = 0.05 [Cadek, (1988)]. Other models predict stress thresholds as high as 70% of the Orowan stress. Thus in the present case where the Orowan (shear) stress = 8.5 MPa, the range in threshold (shear) stress is 0.4 to 6 MPa depending on the model used. This corresponds to a uniaxial tensile stress of about 1 to 12 MPa which is within the range observed. Preliminary examination of post-crept Nb-1wt%Zr-0.1wt%C alloy specimens has not been able to confirm the particular mechanism of the origin of the observed stress threshold. The only significant microstructural feature readily apparent is a pronounced cellular substructure (discussed below). No distinct particle-dislocation interactions have been observed which could be attributed to a dislocation detachment threshold mechanism.

4.2   Activation energy for creep determination

One of the most significant characteristics of creep behavior at temperatures greater than $0.4\ T_m$ is the strong dependence of strain rate on temperature. This is clearly predicted by the Arrhenius relation described by equation (1) where temperature (T) appears in the denominator of the exponential term. A strong dependence on activation energy (Q_c) for creep is also evident in equation (1). Experimental determination of the activation energy for creep thus allows for the identification of the specific mechanism controlling the strain rate.

One of the most precise and frequently used experimental methods to determine the activation energy of creep relies on the temperature dependence of steady state strain rate for various applied constant stresses. If it is assumed that the steady-state strain rate $\dot{\varepsilon}_{ss}$ is a function of only stress and temperature, the following relation can be used to determine the activation energy Q_c:

$$Q_c = \left[\frac{\partial \ln \dot{\varepsilon}_{ss}}{\partial(-1/kT)}\right]_\sigma \qquad (5)$$

Thus, the activation energy Q_c can be obtained as the slope of $\ln\dot{\varepsilon}_{ss}$ versus $1/kT$ plot. In some cases the relation of $\ln\dot{\varepsilon}_{ss}$ versus $1/kT$ will be non-linear indicating that the possibility of two different deformation mechanisms contribute the to the strain rate to a comparable extent. Caution must be observed to assure that steady-state creep has been achieved at the temperature and stress condition imposed. In the present case, such a plot is linear as illustrated in Fig. 7. The activation energy for creep of Nb-1wt%Zr-0.1wt%C falls in the range of 400 to 450 kJ/mole. This may be compared to the value of 401 kJ/mole for the activation energy of self diffusion in niobium [Stuart, 1984)]. This comparison indicates that diffusional processes are strain rate controlling over the stresses and temperatures examined.

4.3 Loss of creep strength at higher temperatures - particle growth

Creep testing at temperatures higher than 1300 K has shown somewhat anomalous behavior. Steady-state strain rates measured early on in a creep test at temperatures > 1400 K typically are lower than strain rates measured several tens of hours later at the same temperature and stress level. Figure 8 illustrates this effect captured during the creep of a specimen at stresses from 30 to 80 MPa at 1400 K.

Particle size measurements have identified that some particle growth has occurred at this temperature for specimens crept > 60 hours. Conversely, no particle growth has been measured on specimens crept for > 500 hours at 1300 K. This growth in mean particle size results in an increase in particle spacing for a given volume fraction of particles which consequently reduces the materials creep resistance. Figure 9 shows the change in mean particle size for specimens crept at 1400 K for >60 hours.

At higher temperatures (> 1400 K in this case), the relatively high interfacial energy of the incoherent particles contributes to the loss in creep strength due to particle growth. This effect is similar to the softening which results from overaging precipitation strengthened materials.

4.4 Stress reduction tests & internal back stress measurement

The steady state creep behavior of class II materials can be better described using the concept of a "back stress" which acts to reduce the applied stress. Under such a description, the steady state creep rate can be expressed as:

$$\dot{\varepsilon} \propto A'(\sigma-\sigma_b)^n \qquad (6)$$

where σ_b represents the back stress. Back stress arises from long-range interaction of dislocations with cell wall. The term $(\sigma-\sigma_b)$ can be described as an effective stress σ^* which acts to control the deformation.

4.4.1 Measurement technique - strain transient dip test

The technique employed to measure this internal back stress was the strain transient dip test. In this method, load is manually removed from the creep machine (thus stress is reduced) and the strain rate $\dot{\varepsilon}$ is measured immediately following transient at the reduced stress level. The technique assumes that the structure immediately following the transient is the same as before the transient, thus allowing a correlation of the structural factors affecting the creep behavior. The original load is reapplied and the specimen is allowed to creep further at which time the load (stress) is again reduced by the same amount. For several starting stress levels, a curve is built up of strain rate measured immediately following the transient (called the reduced strain rate; $\dot{\varepsilon}_R$) versus accumulated strain.

For small stress reductions, $\dot{\varepsilon}_R$ is positive indicating that the reduced applied stress is still greater than the back stress. For larger stress reductions, $\dot{\varepsilon}_R$ is negative, indicating that the reduced applied stress is less than the back stress. Some amount of anelastic back-flow occurs prior to new (lower) steady state strain rate as the dislocation substructure "relaxes" to its new state but is quickly reestablished when the stress is returned to its original value. A parametric approach is then used to find the stress where $\dot{\varepsilon}_R = 0$. This stress defines the back stress for the given conditions of applied stress and temperature.

As determined from stress reductions from initial stress of 53.5 MPa and a temperature of 1434 K, the back stress σ_B is approximately equal to 90% of $\sigma_{applied}$.

4.4.2 Instantaneous strain variation with accumulated strain

The stress cycling tests used to determine the magnitude of the dislocation back stress were also used to examine the instantaneous deformation behavior of the alloy in terms of elastic and plastic strain [Farkas and Mukherjee, (1995)]. Measurements from the stress change tests made during steady-state creep have shown that the total instantaneous strain measured for stress changes exceeded the values calculated from elastic behavior alone. This effect has been identified by previous researchers [Northwood & Smith, (1989), Langdon & Yavari, (1981), and Shi & Northwood, (1993)]. Our research has extended this examination to show how the instantaneous strain (composed of an elastic and plastic component) varies with accumulated strain. The general response can be summarized in the following points:

1. The instantaneous strains from the stress additions were typically larger than the instantaneous strains for the stress reduction near the same approximate accumulated strain value.
2. The total instantaneous strain decreased with accumulated strain even though the magnitude of the stress change was held constant for a given set. This effect has not been reported in previous literature.
3. The difference between the instantaneous strains from a stress addition and a stress reduction for a given $\Delta\sigma$ decreases as $\Delta\sigma$ increases. The implication here is that the mobility of dislocations is impeded in the reverse direction unless the magnitude of stress reduction exceeds the value of internal stress.

11

The apparent work hardening rate **H** was calculated from the stress cycling tests using the expression [Northwood & Smith, (1989)]:

$$\Delta H = \frac{\Delta \sigma}{\Delta \epsilon_{(plastic)}^{instantaneous}} \qquad (7)$$

The true work hardening rate **h**, was then found by extrapolating the plot of log H versus $\Delta \sigma$ as $\Delta \sigma \rightarrow 0$. The value determined for the true work hardening rate h was approximately 7 GPa, or if expressed as a fraction of the elastic modulus, (E = 100 GPa for pure Nb at the test temperature), h/E $\approx$ 0.07. This value was found to be fairly constant even though the instantaneous strain produced from a stress change decreased with accumulated strain. We have included our paper discussing these experiments as Appendix C.

4.5 Microstructural correlation with creep behavior

As indicated in the previous section, a dislocation substructure develops in class II alloys during the primary creep transient which eventually reaches a "steady-state". This substructure initially is rather heterogeneous because it is influenced by grain boundaries and neighboring grain misorientation. Consequently, measurement of the substructure's quantitative characteristics is difficult. Figure 10 shows a series of TEM micrographs taken from samples of Nb-1wt%Zr-0.1wt%C after creep at a relatively high stress level. As expected, the substructure produced takes the form of subgrains whose walls form a tight knit array of dislocations. The subgrain interior remains relatively free of dislocations.

A typical class II alloy undergoing primary creep is characterized by a pronounced heterogeneization of its dislocation distribution. The original matrix grains become fragmented into subgrains. As primary creep proceeds, the substructure spreads over the whole volume of the specimen and a three-dimensional heterogeneous network forms consisting of relatively coarse equiaxed subgrains. The heterogeneity successively diminishes as small subgrains coarsen and larger subgrains become refined until a relatively uniform distribution of subgrains (both in size and shape) results. The steady state structure is characterized by rather time invariant parameters related primarily to the applied stress level.

The diminishing primary creep strain rate is associated with a decrease in effective stress σ^* which is due to a growth in the long-range internal or dislocation back stress. The growth in internal stress which occurs during primary creep is related to the growth in total dislocation density. Since the majority of dislocations end up as part of the subgrain cell wall, the substructure obviously contributes to the internal stress substantially.

12

The generally accepted conclusion, based on numerous experimental results shows that the mean subgrain size is related to the applied stress according to [Takeuchi & Argon, (1976)]:

$$\frac{d_s}{b} = K_d \frac{G}{\sigma}$$

(8)

where d_s is the subgrain dimension, σ the applied stress, and constant $K_d \approx 10.5$. Figure 11 is a plot of measured subgrain sizes from crept Nb-1wt%Zr-0.1wt%C alloy superimposed with a plot of equation (8) using the known parameters of Burger's vector and shear modulus. The correspondence between measured subgrain size and predicted is good.

Superimposed on Fig. 11 is the range of grain size measured for one of the specific heat treatments provided (1 hr at 1755 K + 2 hr at 1477 K). From this comparison, it can be seen that the predicted subgrain size is smaller than the mean grain size for stress levels greater than approximately 10 MPa. Thus at stress levels greater than 10 MPa, no grain size effects would be expected in the alloys high-temperature deformation behavior. Only when the actual grain size is on the order of the subgrain size (developed during primary creep at the specified stress level) would any grain size effects be present. This explains why no difference in high-temperature creep behavior was observed for the two heat treatments examined.

Of particular interest is that equation (7) predicts subgrain sizes on the order of 10 microns for stress levels near our predicted stress threshold. This value is within the range of measured grain size for one of the heat treatments.

4.6   Thermodynamic analysis of particle formation and stability

The generally observed carbides produced during heat treatment of Nb-1Zr-0.1C occur as three forms; Nb_2C, NbC and ZrC [Grobstein and Titran, (1986)]. The thermodynamic driving force for the formation of any particular carbide form can be determined by comparing each reaction's Gibbs free energy at the desired reaction temperature. It will be shown that Nb_2C has the lowest Gibbs free energy when the alloy constituents are present in a homogeneous mixture, a condition which occurs during solution treatment at elevated temperature. This thermodynamic analysis supports the experimental observation of Nb_2C forming first during the heat treatment [Grobstein and Titran, (1986)]. Nb_2C is metastable however, and the final form of carbide which *evolves* during aging is a mixture of the monocarbides NbC and ZrC. Both NbC and ZrC are of the same fcc crystal type and display complete solid solubility thus a free energy of mixing can be determined at any desired temperature and mixture concentration. Calculations show that the Gibbs free energy of the mixed monocarbides of NbC and ZrC crosses the free energy curve of Nb_2C formation. An equilibrium condition occurs when the free energy of Nb_2C equals that of the NbC + ZrC mixture. This equilibrium condition also fixes the NbC-to-ZrC concentration at any particular aging temperature.

4.6.1 Calculating reaction free energies for pure components.

The reactions of niobium and zirconium with carbon discussed above can be represented by:

$$2Nb + C = Nb_2C \tag{9}$$

$$Nb + C = NbC \tag{10}$$

$$Zr + C = ZrC \tag{11}$$
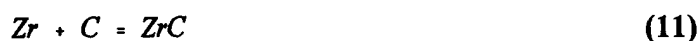
where in this case, pure components are reacting to form pure carbide products. For each carbide, the reaction standard Gibbs free energy ($\Delta G^0_{reaction}$) can be computed from:

$$\Delta G^0_{reaction} = \Delta G^0_{products} - \Delta G^0_{reactants} \tag{12}$$

The numerical value of Gibbs free energy for a selected reaction can easily be calculated from the published values for individual components listed in thermodynamic data handbooks [Knacke, Kubachewski and Hesselmann, (1991)]. This is easily facilitated with a spreadsheet program which allows mathematical calculations of columnar data.

Figure 12 shows such a free energy diagram for the reactions (9) to (11) involving pure components. As can be seen, $\Delta G^0 < 0$ for all carbide formation reactions involving Nb and Zr throughout the temperature range examined (300 K to 2000 K). Values of $\Delta G < 0$ indicate that the reactions are thermodynamically favored in the direction written ie., occur spontaneously. The more negative the value of ΔG, the greater the driving force to complete the reaction and the greater the tendency for this reaction to occur (greater stability) when compared to a reaction with a lesser negative value of ΔG. (It must be noted here that although free energy values can be used to examine the relative driving force for a reaction to occur, kinetics still controls the rate at which a reaction takes place.) Of particular interest is that the formation of ZrC from its pure components has the lowest ΔG^0 indicating that it is more stable at equilibrium than any of the other carbides throughout the temperature range *contrary* to observation. As will be shown, a component's presence in dilute solution significantly affects the reaction free energy result.

4.6.2 Calculating reaction free energies of non-pure components

The actual reactions do not involve pure reactants or do not necessarily produce pure product carbides. In order to examine the formation of carbide precipitates within the alloy during heat treatment, it is necessary to use the thermodynamic reaction equilibrium criteria for systems containing components in condensed solution [Gaskell, (1981)]. In this case, where the components are present in solution, the Gibbs free energy ($\Delta G_{reaction}$) of the reaction (not in its standard state) is computed from:

14

$$\Delta G_{reaction} = \Delta G^0_{reaction} + RT \ln Q \tag{13}$$

where Q is termed the activity quotient and requires knowledge of the components thermodynamic activities at the reaction temperature. It becomes necessary to calculate (or estimate) the activity of carbon, zirconium, and niobium as a function of temperature and time during the formation and evolution of the carbides formed.

As an example for the formation of ZrC as described in reaction (11), the activity quotient Q may be written as the ratio of the activities of the products to the activities of the reactants:

$$Q = [\frac{a_{ZrC}}{a_{Zr}a_C}] \tag{14}$$

The Gibbs free energy is altered by the amount RTlnQ and has the effect of rotating the free energy line as shown in Fig. 13. For the zirconium-carbon reaction example, having either or both reactants (Zr and/or C) in dilute solution (activity <1) rotates the free energy line anti-clockwise, increasing the value of ΔG for a given temperature. The free energy line rotates clockwise if the product (ZrC) forms as a dilute solution in another component. The difference in free energy between the reaction occurring with components in condensed solution and the pure reaction energy at a given temperature results from the effect of component activity on the reaction. Reaction product stabilities can thus be significantly altered when the components are in solution vice pure. The activity values become a significant factor in these predictions.

As stated earlier, the activity of the reaction components must be considered when components react while in solution as will be the case for carbide formation within the alloy matrix during heat treatment. The activities of the components are functions of composition and temperature and are expected to vary as the reactions proceed. In this analysis, several methods where examined to estimate the component activities.

As a first estimate, ideal (Rauoltian) behavior was assumed. The activity of each component is then equal to its mole fraction:

$$a_i = X_i \tag{15}$$

where X_i is the mole fraction of the species i. For the alloy Nb-1wt%Zr-0.1wt%C, the mole fractions (X_i) were determined and thermodynamic activities (a_i) were initially estimated to be:

$$a_{Nb} = 0.9823$$
$$a_{Zr} = 0.0101$$
$$a_C = 0.0077$$

15

These initial estimates for the activities of Nb and Zr can be taken with some validity because Nb and Zr display complete solid solubility in the temperature range considered. Carbon activity however is significantly different from this estimate based on mole fraction. Both solubility data of carbon in Nb [Smith, Carlson, & De Avillez, (1987)] and a method using defect interaction energies [Hoch, (1967)] show that the activity of carbon (in Nb) is very nearly equal to one for all temperatures less than 1600 K.

The formation of ZrC in this reaction may be considered to be pure since it appears as a precipitate particle (and forms separate from the alloy matrix). Thus the activity of precipitated (pure) ZrC; $a_{ZrC} = 1$. The mixed (NbC + ZrC) carbide activity was estimated from the ZrC-to-NbC ratio present. For example, for a ZrC/NbC ratio of 2:1, the ideal activities are equivalent to the mole fraction of the components in the complex carbide; $a_{ZrC} = 0.66$ and $a_{NbC} = 0.33$.

4.6.3 Carbide formation

The Nb-1Zr-0.1C alloy is typically prepared by vacuum-consumable-arc melting of the constituents followed by casting to an ingot form [Stuart, (1984)]. Various fabrication methods are then used to produce the final form (sheet or rod) of the commercial alloy. Typically, the ingot is canned prior to high-temperature extrusion to preclude oxygen contamination, extruded then either room temperature swaged (cold worked) or hot rolled to desired thickness. A final anneal is given to equilibrate the microstructure and produce the desired grain size.

During melting and follow-on extrusion, the alloying agents are homogenized and will generally remain in solution with thermodynamic activities predicted as in the previous discussion, ie., the activity of each component being approximately equal to its mole fraction (assuming ideal solution behavior). Under these conditions, the reaction free energy of each of the carbides will be as shown in Fig. 14. Since the 1wt% zirconium is now in dilute solution, its respective ZrC free energy curve is rotated anti-clockwise placing it above the free energy curve of Nb_2C. Nb_2C formation has the lowest free energy at all temperatures greater than 600 K consequently it forms first as demonstrated experimentally.

Nb_2C formation occurs rapidly as the temperature is lowered during the alloy processing. In fact, rapid cooling rates such as experienced by quenching in liquid tin at 600 K must be employed to suppress Nb_2C precipitation [Ostermann and Bollenrath, (1969)]. Subsequent aging (either as a deliberate step or during the anneal) transforms the Nb_2C to the mixed monocarbide NbC + ZrC. The final form is often referred to as a complex carbide written as (Nb,Zr)C [Grobstein and Titran, (1986)]. In order to show thermodynamically how this is possible, the free energy of mixing of a solid solution of NbC + ZrC must be examined.

The free energy of mixing of a solid solution can be expressed as the sum of the enthalpy or heat of mixing and the product of the temperature and entropy of mixing:

$$\Delta G_{mixing} = \Delta H_{mixing} - T\Delta S_{mixing} \tag{16}$$

16

In this case, ideal solution behavior is again assumed where by the heat of mixing is zero:

$$\Delta H_{mixing} = 0 \tag{17}$$

and the entropy of mixing is given by:

$$\Delta S_{mixing} = -R \ (X_A \ \ln X_A + X_B \ \ln X_B) \tag{18}$$

The free energy values at any temperature for pure NbC ($X_{NbC} = 1$) and pure ZrC ($X_{NbC} = 0$) were previously determined and plotted in Fig. 12. The free energy of the monocarbide mixture (NbC + ZrC) can be determined from equations (16) and (18) and plotted on a three-dimensional graph of free energy, temperature, and NbC concentration. In this way the driving force for transformation of Nb_2C to the NbC+ZrC mixture can be examined more fully.

This method was employed to illustrate the evolution of the free energy of the NbC+ZrC mixture during solution treatment and subsequent aging as a function of NbC content (of the particles). Figure 15 shows two intersecting surfaces, one specifying the free energy of Nb_2C, and the other depicting the free energy of the mixed monocarbide (NbC + ZrC) when the activity of Zr is low as during initial solution treatment. The curvature of the mixed monocarbide free energy surface becomes more pronounced at higher temperatures due to the effect of the entropy of mixing term in equation (16).

The locus of points determined by the intersection of both surfaces determines the *equilibrium* condition of the two phases (Nb_2C and the mixed monocarbide) for any temperature. Equilibrium in this case indicates that the two phases can coexist at the specified NbC concentration of the mixed monocarbide. The locus of points determined by the intersection of the two surfaces also specifies the *maximum* NbC concentration that may exist at equilibrium with Nb_2C. This also predicts that there remains a driving force for transformation of Nb_2C to a mixed monocarbide of lower NbC concentration (higher ZrC concentration) or a driving force exists for the increase in ZrC concentration in a given NbC+ZrC mixture. In this case (Fig. 15), the Nb_2C phase displays a lower free energy surface for all but a small portion of the temperature-NbC concentration region.

Figure 16 extends the NbC+ZrC mixture free energy to its "pure" components (where the activities = 1). This may be regarded as the limit of the free energy for a given NbC concentration (of the mixed monocarbide) and temperature.

4.6.4 Comparison of predicted equilibrium lattice parameter of NbC+ZrC with experiment.

The locus of points of the two intersecting free energy surfaces can be used to determine the equilibrium NbC-to-ZrC ratio that is produced during aging of the alloy. Vegard's relation for the NbC + ZrC solid solution shows little deviation from linearity [Norton and Mowrey, (1949)] and the NbC concentration of the mixture can be used to predict the mixture's lattice parameter. A problem arises in predicting the lattice parameter of the mixture in that both NbC and ZrC

17

display a *range* in their lattice parameters depending on carbon content of the non-stoichiometric species [Smith, Carlson & DeAvillez, (1987) and Fromm & Jehn, (1972)]. Figure 17 is a plot of predicted lattice parameter of the NbC + ZrC mixture at equilibrium (from the intersection of surfaces in Fig. 16) compared to measured lattice parameters our alloy and of a similar alloy at different aging temperatures. This prediction is based on using values of the lattice parameter from the stoichiometric (ie., 1-to-1 atom relation) NbC and ZrC components.

Although some deviation is present in the correlation, the general trend is similar in that at higher aging temperatures, smaller lattice parameter of the mixture is predicted and observed. This correlates to a higher NbC concentration in the mixture with higher aging temperatures. It should be noted here that since excess Zr remains in solution for this alloy chemistry, there will always remain a driving force for increasing the ZrC concentration of the (NbC+ZrC) mixture even when all Nb_2C has been transformed. The final lattice parameter of the mixture must then depend on aging time as well as aging temperature. This final point remains to be shown experimentally.

4.6.5 Model for transformation of Nb_2C to (NbC+ZrC) mixture

The thermodynamic analysis presented above allows development of a model for the transformation of Nb_2C to the NbC+ZrC mixed monocarbide. The significance of this model is that the "larger blocky" Nb_2C carbides that form early in the thermomechanical processing of the alloy are refined to a more homogeneous distribution of small precipitates (of the mixed monocarbide). The consequences of this directly enhances the high-temperature mechanical properties of the alloy since small evenly distributed particles are a necessary prerequisite for improved creep resistance.

Figure 18 illustrates the sequence of events in this model for the transformation of Nb_2C to the finely dispersed mixed carbide of NbC + ZrC. The most significant aspect of this sequence is that the zirconium distribution does not remain homogeneous (consequently its thermodynamic activity increases). Experimental microprobe analysis supports this aspect in that elevated zirconium concentrations have been identified around large particles of Nb_2C [Arzamasov & Vasil'eva, (1978)]. It can be envisioned that the free energy surface of the NbC+ZrC mixture of Fig. 15 bends downward approaching that depicted in Fig. 16 as the zirconium concentration (activity) increases. In the limit, the free energy condition of Fig. 16 is reached. The exact nature of why zirconium concentrates near the Nb_2C particles remains subjective although it may be due to internal stress effects experienced by the misfit of the larger zirconium atoms in the niobium matrix.

5. Conclusions

The monotonic creep behavior of a precipitation strengthened niobium alloy (Nb-1wt%Zr-0.1wt%C) is comparable with 1wt% Zr niobium alloy (at high stresses) and is superior to pure niobium. The alloy's low-stress creep behavior points to the existence of a stress threshold below 16 MPa. A calculation of the Orowan stress for particle dislocation bypass based on the statistical particle size and spacing supports the observed approach to a threshold stress for creep at a temperature of 1300 K.

18

Creep testing performed at higher temperatures (>1400 K) has identified a reduction in strength (ie., higher steady-state creep rate) with time at temperature. The higher steady-state creep rates only appear after several tens of hours under constant load. The loss of creep strength has been attributed to the growth and subsequent increased mean spacing of carbide particles in the matrix.

Stress reduction tests have shown that the internal dislocation back stress is a significant portion of the applied stress. The measured back stress at an applied stress of 50 MPa is approximately 90% of the applied stress. The back stress arises from the long-range interaction of dislocations with the cell walls formed during the primary creep of the alloy.

A distinct substructure forms during primary creep. This substructure takes the form a cellular array of dislocation tangles and is typical of all Class-II creep materials. Cell interiors remain relatively dislocation free. The measured cell dimensions are consistent with measurements of Nb-1wt%Zr performed under the previous research grant. The dislocation cell dimensions have been shown to be inversely related to the applied stress. Relatively little dislocation-particle interaction has been identified at the stress levels examined.

A thermodynamic analysis of particle formation and stability was performed which supports the observed transformation of Nb_2C to a mixture of ZrC and NbC during heat treatment. Free energy calculations shows that a maximum NbC concentration (in the mixed carbide particles) exists for a given aging temperature. Higher aging/annealing temperatures produce a greater equilibrium NbC content in the particles. A model was developed of the carbide formation which is useful in predicting the alloy's creep properties.

6.   Personnel - Degrees Awarded

The following personnel were primarily involved in the work of this research program:

Professor Amiya K. Mukherjee, Principal Investigator
Dr. Hong Sheng Yang, Visiting Assistant Researcher
Dr. Koji Tanaka, Visiting Assistant Researcher
Dr. Rajiv Mishra, Visiting Assistant Researcher
Dr. Michael J. Davidson, Ph.D. awarded July 1992
Randy B. Grishaber - M.S. degree awarded September 1993
David M. Farkas - Ph.D. degree to be completed June 1995

## 7.	References

Arieli, A. and Mukherjee, A. K., Proc. Int. Conf. on Creep, Ed. B. Wilshire and D.R.J. Owen, Pineridge Press, Swansea, U.K., p. 97, (1981).

Arzamasov, V. B., and Vasil'eva, E. V., Metal Science and Heat Treatment, 4, p. 291, (1978).

Cadek, J., Creep in Metallic Materials, Elsevier, N.Y, (1988)

Davidson, M. J., Biberger, M. and Mukherjee, A. K., Scripta Met. Material., Vol 27, p. 1829, (1992).

Delgrosso, E. J., Carlson, C. E. and Kaminski, J. J., Journal of the Less-Common Metals, 12, p. 173 (1967).

Farkas, D. M. and Mukherjee, A. K., Scripta Met. Material., Vol 32, (1995).

Fromm, E., and Jehn, H., Met. Trans, Vol. 3, p. 1685, (1972).

Gaskell, D.R., Introduction to Metallurgical Thermodynamics, Hemisphere Publishing, (1981).

Grobstein, T. L., and Titran, R. H.,   DOE/NASA/16310-6, NASA TM-100848, (1986).

Hoch, Phase Stability in Metals and Alloys, (1967).

Knacke, Kubachewski and Hesselmann (Ed.), Thermodynamic and Chemical Properties of Inorganic Substances, 2nd Ed., (1991).

Langdon, T. G. and Yavari, P., Creep and Fracture of Engineering Materials and Structures, Proceedings of the International Conference, Swansea, p 71 (1981).

Northwood, D. O. and Smith, I. O., Phys. Stat. Sol. (a) 115, p. 125 (1989).

Norton, J. T., and Mowry, A. L., Metals Transactions, p. 133, Feb., (1949).

Ostermann, F., and Bollenrath, F., High Temperature Materials, Plansee Seminar, Springer Verlag, Wien, N.Y., p. 317, (1969).

Shi, L. and Northwood, D. O., Phys. Stat. Sol. (a) 137, p. 75 (1993).

Smith, J. F., Carlson, O. N., and De Avillez, R. R., Journal of Nuclear Materials, 148, p. 1, (1987).

Stuart, H., Niobium: Proceedings of the 1981 International Symposium, American Institute of Mining, Metallurgical, and Petrolium Engineers, Inc., (1984).

Takeuchi, S. and Argon, A. S., J. Mater. Sci., 11, p. 1542, (1976).

Titran, R. H., Moore, T. J., and Grobstein, T. L., DOE/NASA report TM-16310-3, (1987).

Yeh, Y. H., Nakashima, H., Kurishita, H., Goto, S., and Yoshinaga, H., Materials Transactions, JIM, Vol. 31, No. 4, p. 284, (1990).

8.   Cumulative List of Publications Resulting from AFOSR Support

A-1   PUBLISHED

1980

1.   LOW STRESS AND SUPERPLASTIC CREEP BEHAVIOR OF Zn-22% Al EUTECTOID ALLOY,
A. Arieli, A. K. S. Yu, and A. K. Mukherjee, Metallurgical Transactions, Vol. 11A, pp. 181-191, 1980.

2.   FACTORS AFFECTING THE MAXIMUM ATTAINABLE DUCTILITY IN A SUPERPLASTIC TITANIUM ALLOY,
A. Arieli and A. Mukherjee, Materials Science and Engineering, Vol. 43, pp. 47-54, 1980.

3.   HIGH-TEMPERATURE DIFFUSION-CONTROLLED CREEP BEHAVIOR OF THE Zn-22% Al EUTECTOID TESTED IN TORSION,
A. Arieli and A. K. Mukherjee, Acta Metallurgica, Vol. 10, pp. 1571-1581, 1980.

1981

4.   AN EVALUATION OF THE EFFECTS OF CONCURRENT GRAIN GROWTH DURING SUPERPLASTIC FLOW OF THE Ti-6Al-4V ALLOY,
A. Arieli, B. J. Maclean and A. K. Mukherjee, Proc. of the 4th Intn'l. Conf. on Titanium, Kyoto, Japan, Ed. H. Kimura and O. Izumi, pp. 1047-1056, 1981.

5.   TWO-AND THREE-DIMENSIONAL DEFORMATION MECHANISM MAPS FOR HIGH TEMPERATURE CREEP OF Zn-22% Al EUTECTOID ALLOY,
A. Arieli and A. K. Mukherjee, Materials Science and Engineering, Vol. 47, pp. 113-120, 1981.

6.   REPLY TO "A CRITICAL EVALUATION OF THE CONCEPT OF A UNIVERSAL PARAMETER TO UNIQUELY SPECIFY HIGH TEMPERATURE CREEP MECHANISMS,"
A. Arieli and A. K. Mukherjee, Scripta Metallurgica, Vol. 15, Sept. 81, p. 1053, 1981.

1982

7.   THE EFFECT OF STRAIN AND CONCURRENT GRAIN GROWTH ON THE SUPERPLASTIC BEHAVIOR OF THE Ti-6Al-4V ALLOY,
A. Arieli, B. J. McLean and A. K. Mukherjee, Res Mechanica, Vol. 6, pp. 131-159, 1982.

1983

8.   ELEVATED TEMPERATURE CAVITATION IN CREEP AND SUPERPLASTICITY OF Ti-6Al-4V ALLOY,
G. Gurewitz, N. Ridley and A. K. Mukherjee, Proceedings of the International Conference on Fracture Mechanics, Nov. 1983, Pub. by the Chinese Soc. of Theoretical and Applied Mech., p. 898, Science Press, Beijing, China, 1983.

1984

9   MECHANICAL AND MICROSTRUCTURAL ASPECTS FOR OPTIMIZING THE SUPERPLASTIC DEFORMATION OF Ti-6Al-4V ALLOY,
B. Hidalgo-Prada, G. Gurewitz and A. K. Mukherjee, Proceedings of Intn'l Amer. Conf. on Mat. Tech., San Juan, Puerto Rico, Ed, D. Black, p. 18.1, 1984.

10.   A METALLOGRAPHIC STUDY OF CAVITATION IN Ti-6Al-4V ALLOY,
G. Gurewitz and A. K. Mukherjee, Advances in Fracture Research, Ed., S. R. Valluri, et al., Pergamon Press, Oxford, p. 2319-2324, 1984.

1985

11.   CREEP AND DISLOCATION SUBSTRUCTURE,
L. Bendersky, A. Rosen and A. K. Mukherjee, Invited Review, International Metals Review, Vol. 30, p. 1, 1985.

12.   THE STRAIN RATE SENSITIVITY VALUES IN SUPERPLASTIC DEFORMATION,
G. Gurewitz and A. K. Mukherjee, Materials Science and Engineering, Vol. 70, p. 191-196, 1985.

13.   MICROSTRUCTURAL EVOLUTION DURING SUPERPLASTIC DEFORMATION IN A Ni-MODIFIED Ti-6Al-4V ALLOY,
B. Hidalgo-Prada and A. K. Mukherjee, Scripta Metallurgica, Vol. 19, pp. 1235-1239, 1985.

14.   SUPERPLASTICITY-CORRELATION BETWEEN STRUCTURE AND PROPERTIES,
M. Suery and A. K. Mukherjee, Creep Behavior of Crystalline Solids, ed. B. Wilshire, Pineridge Series on Progress in Creep and Fracture, Pineridge Press, Swansea G.B., pp. 137-200, 1985.

15.   CORRELATION BETWEEN MECHANICAL PROPERTIES AND MICROSTRUCTURE IN A NI-MODIFIED SUPERPLASTIC Ti-6Al-4V ALLOY,
B. Hidalgo-Prada and A. K. Mukherjee, Proc. of Intn'l. Conf. of Strength of Metals and Alloys-7, Montreal Canada, ed. H. J. McQueen et al., Vol. 2, pp. 835-840, 1985.

1986

16.   CAVITY NUCLEATION IN 7475 AL ALLOY,
M. K. Rao and A. K. Mukherjee, Scripta Met., Vol. 20, pp. 411-414, 1986.

17.   REVIEW: CAVITATION BEHAVIOR DURING HIGH TEMPERATURE DEFORMATION OF MICROGRAINED SUPERPLASTIC MATERIALS,
B. P. Kashyap and A. K. Mukherjee, Invited review, Res Mechanical, Vol. 17, pp. 293-355, 1986.

1986

18. SUPERPLASTIC DEFORMATION BEHAVIOR OF A FINE-GRAINED 7475 Al ALLOY,
B.P. Kashyap, A. Arieli and A. K. Mukherjee, Materials Science and Engineering, Vol. 80, pp. 181-193, 1986.

1987

19. ON THE TRANSITION FROM SUPERPLASTIC TO NON-SUPERPLASTIC DEFORMATION AT HIGH STRAIN RATES,
Atul Chokshi and Amiya Mukherjee, Scripta Met, Vol. 20, pp. 1771-1774, 1987.

20. ON THE EVALUATION OF PARAMETERS OF THE CONSTITUTIVE EQUATION FOR 7475 AL ALLOY,
M. Rao and A. K. Mukherjee, Journal of Materials Science, Vol. 22, pp. 459-465, 1987.

21. A REPLY TO DISCUSSION OF CAVITATION STUDY IN INGOT AND POWDER METALLURGICALLY PROCESSED SUPERPLASTIC Al-Li ALLOYS,
M.C. Pandey, J. Wadsworth and A. K. Mukherjee, Materials Science and Engineering, Vol. 89, pp. 71-173, 1987.

22. SUPERPLASTIC DEFORMATION IN AN AL-Li ALLOY,
A. Chokshi, A. K. Mukherjee, Proc. of International Conference on Metallurgy and Materials Science, pp. 265-272, 1987, Ed. S.I. Andersen, et al., Denmark.

23. HIGH STRAIN RATE SUPERPLASTICITY IN MECHANICALLY ALLOYED ALUMINUM,
T. R. Bieler, T. G. Nieh, J. Wadsworth and A. K. Mukherjee, Proceedings of IX Inter-American Conference on Materials Technology, Santiago, Chile, Ed. Univ. of Chile, pp. 213-217, 1987.

24. MICROSTRUCTURAL EVIDENCE FOR DYNAMIC RECRYSTALLIZATION DURING SUPERPLASTIC DEFORMATION,
Atul H. Chokshi, Jeffrey Wadsworth and Amiya K. Mukherjee, Scripta Met., Vol. 21, pp. 1347-1351, 1987.

25. EFFECT OF HYDROSTATIC PRESSURE ON HIGH TEMPERATURE FAILURE IN SUPERPLASTIC ALUMINUM ALLOYS,
A. H. Chokshi, J.E. Franklin and A. K. Mukherjee, Mechanical Behavior of Materials, Ed. M.G. Yan, et al., Vol. 1, pp. 461-468, 1987.

26. ON CONTROL OF CAVITATION IN AN Al-Li BASED ALLOY DURING SUPERPLASTIC FORMING,
M. C. Pandey and A. K Mukherjee, Indian Journal of Technology, Vol. 25, pp. 579-585, 1987.

1988

27. ON THE INTER-DEPENDENCE OF GRAIN BOUNDARY PHENOMENON AND SUPERPLASTIC DEFORMATION,
B. P. Kashyap and A. K. Mukherjee, Fundamentals of Diffusion Bonding, Ed. Y. Ishida, Elsevier, Amsterdam pp. 397-420, 1988.

28. A TOPOLOGICAL STUDY OF SUPERPLASTIC DEFORMATION IN AN AL-Li ALLOY WITH A BIMODAL GRAIN SIZE DISTRIBUTION,
A. H. Chokshi and A. K. Mukherjee, Metallurgical Transactions, Vol. 19A, p. 1621, 1988.

29. SUPERPLASTIC-LIKE BEHAVIOR AT HIGH STRAIN RATES IN A MECHANICALLY ALLOYED ALUMINUM,
T. R. Bieler, T. G. Nieh, J. Wadsworth and A. K. Mukherjee, Scripta Met., Vol. 22, pp. 81-86, 1988.

30. SUPERPLASTICITY IN A MECHANICALLY ALLOYED MATRIX,
T. R. Bieler and A. K. Mukherjee, Invited paper, XXII International Metallurgy Congress, Bologna, Italy, Vol. 1, pp. 485-503, 1988.

31. SUPERPLASTICITY IN SILICON CARBIDE REINFORCED ALUMINUM AND MECHANICALLY ALLOYED ALUMINUM AEROSPACE ALLOYS,
A. H. Chokshi, T. R. Bieler, T. G. Nieh, J. Wadsworth and A. K. Mukherjee, Superplasticity in Aerospace, Ed. H. C. Heikkenen, et al., A.I.M.E., Warrendale, PA., pp. 229-245, 1988.

32. CAVITATION FAILURE IN SUPERPLASTIC ALLOYS,
A. H. Chokshi and A. K. Mukherjee, Superplasticity in Aerospace, Ed. H. C. Heikkenen, et al., A.I.M.E., Warrendale, PA., pp. 167-182, 1988.

33. ON THE EFFECTS OF HYDROSTATIC PRESSURE ON MECHANICAL PROPERTIES OF 7475 ALUMINUM ALLOY,
J. E. Franklin, J. Mukhopadhyay and A. K. Mukherjee, Scripta Metallurgica, Vol. 22, pp. 865-870, 1988.

34. THE SUPERPLASTIC-LIKE CHARACTERISTICS OF A SILICON CARBIDE WHISKER REINFORCED ALUMINUM COMPOSITE,
A. H. Chokshi, T. G. Nieh, J. Wadsworth and A. K. Mukherjee, Strength of Metals and Alloys, Ed. P. O. Kettunen, et al., Pergamon Press, Vol. 1, p. 301, 1988.

35. SUPERPLASTIC BEHAVIOR OF MECHANICALLY ALLOYED ALUMINUM IN90211,
T. R. Bieler and A. K. Mukherjee, Strength of Metals and Alloys, Ed. P. O. Kettunen, et al., Vol. 1, pp. 289-294, 1988.

36. THRESHOLD STRESS AND SUPERPLASTIC BEHAVIOR OF MECHANICALLY ALLOYED ALUMINUM IN90211,
T. R. Bieler and A. K. Mukherjee, Mechanical and Physical Behavior of Metallic and Ceramic Composites, Ed. S. I. Anderson, et al., Riso, Denmark, pp. 297-302, 1988.

1988

37. PARTICLE CHARACTERIZATION AND CAVITY NUCLEATION DURING SUPERPLASTIC DEFORMATION IN AL-Li BASED ALLOYS,
M. C. Pandey, J. Wadsworth and A. K. Mukherjee, Journal of Materials Science, Vol. 23, p. 3509, 1988.

38. ENHANCED PLASTICITY OF MECHANICALLY ALLOYED ALUMINUM IN90211,
T. R. Bieler, T. G. Nieh, J. Wadsworth and A. K. Mukherjee, Symposium I on "Interfacial Structure, Properties and Design, Materials Research Society, Vol. 120, pp. 137-142, 1988.

39. THE ROLE OF GRAIN BOUNDARIES IN THE DEFORMATION AND FAILURE OF A SUPERPLASTIC Al-Li ALLOY,
A. H. Chokshi and A. K. Mukherjee, in "Interfacial Structure, Properties and Design", Materials Research Society, Vol. 122, pp. 413-418, 1988.

1989

40. THE ROLE OF CAVITATION IN THE FAILURE OF SUPERPLASTIC ALLOYS,
A. H. Chokshi and A. K. Mukherjee. In: Superplasticity and Superplastic Forming, Eds. C.H. Hamilton and N.E. Paton, TMS-AIME, Warrendale, PA, pp. 149-159, 1989.

41. HIGH RATE SUPERPLASTIC BEHAVIOR OF MECHANICAL ALLOYED ALUMINUM IN90211,
T. R. Bieler, T. G. Nieh, J. Wadsworth and A. K. Mukherjee. In: Superplasticity and Superplastic Forming, Eds. C. H. Hamilton and N.E. Paton, TMS-AIME, Warrendale, PA, pp. 161-165, 1989.

42. THE CAVITATION AND FRACTURE CHARACTERISTICS OF A SUPERPLASTIC Al-Cu-Li-Zr Alloy,
A. H. Chokshi and A. K. Mukherjee, Materials Science and Engineering, A110, pp. 49-60, 1989.

43. SUPERPLASTICITY IN METALS AND CERAMICS,
A.K. Mukherjee, T. Bieler, and A. Chokshi, Materials Architecture, J.B. Bilde-Sorenson, et. al., Eds., Riso, Denmark, pp. 207-231, 1989.

44. AN ANALYSIS OF CAVITY NUCLEATION IN SUPERPLASTICITY,
A. Chokshi and A. K. Mukherjee, Acta Metallurgica, Vol. 37, pp. 3007-3017, 1989.

45. THE STRAIN HARDENING BEHAVIOR OF SUPERPLASTIC Ti-6A1-4V,
M. Meier and A. K. Mukherjee, Scripta Metallurgica, Vol. 24, pp. 331-336, 1989.

1990

46. EFFECT OF STRAIN AND TEMPERATURE IN A SUPERPLASTIC NiMODIFIED Ti-6A1-4V ALLOY,
B. H. Prada, J. Mukhopadhyay and A. K. Mukherjee, Japan Institute of Metals, Vol. 31, No. 3, pp. 200-226, 1990.

1990

47. THE ROLE OF ADIABATIC HEATING ON HIGH RATE SUPERPLASTIC ELONGATION,
     T. R. Bieler and A. K. Mukherjee, <u>Scripta Metallurgica</u>, Vol. 24, No. 6, pp. 1003-1008, 1990.

48. CORRELATION OF MECHANICAL BEHAVIOR WITH MICROSTRUCTURAL ASPECTS OF Ni MODIFIED SUPERPLASTIC Ti-6Al-4V ALLOY,
     B. Hidalgo-Prada, J. Mukhopadhyay and A. K. Mukherjee, <u>Trans. Japan Metals</u>, Vol. 31, No. 8, p. 689, 1990.

49. THE HIGH STRAIN RATE SUPERPLASTIC DEFORMATION MECHANISMS OF MECHANICALLY ALLOYED ALUMINUM IN90211,
     T. R. Bieler and A. K. Mukherjee, <u>Materials Science and Engineering</u>, Vol. A128, pp. 171-182, 1990.

50. CAVITATION AND FRACTURE OF MECHANICALLY ALLOYED ALUMINUM AT HIGH HOMOLOGOUS TEMPERATURES,
     T. R. Bieler, G. R. Goto and A. K. Mukherjee, <u>Journal of Materials Science</u>, Vol. 25, pp. 4125-4132, 1990.

51. THE ROLE OF HYDROSTATIC PRESSURE IN THE CAVITATION FAILURE OF A SUPERPLASTIC ALUMINUM-LITHIUM ALLOY,
     A. H. Chokshi and A. K. Mukherjee, The Brittle-Ductile Transition in Rocks (The Heard Volume), A. G. Duba, et. al., eds. (American Geophysical Union, Washington, D.C., 1990), p. 83.

52. THE EFFECT OF DEFORMATION MECHANISM(S) ON SUPERPLASTIC ELONGATION OF MECHANICALLY ALLOYED ALUMINUM IN90211,
     A. K. Mukherjee and T. R. Bieler, <u>Structural Applications of Mechanical Alloying</u>, Eds. F. Froes and J. deBarbadillo, ASM, Materials Park, OH (1990) pp. 185-192.

53. NUMERICAL MODELING OF SUPERPLASTIC FORMING OF SHEET METAL DIAPHRAGMS,
     H. S. Yang and A. K. Mukherjee, <u>Proceedings of Superplasticity in Aerospace II</u>, T. R. McNelley and H. C. Heikkenen, Eds., TMS-AIME, Anaheim, CA pp. 103-119, 1990.

54. EFFECT OF HYDROSTATIC PRESSURE ON SUPERPLASTIC DEFORMATION OF Al-Li ALLOY,
     Ho-Sung Lee and A. K. Mukherjee, <u>Proceedings of Superplasticity in Aerospace II</u>, T. R. McNelley and H. C. Heikkenen, Eds., TMS-AIME, Anaheim, CA pp. 121-128, 1990.

55. SUPERPLASTICITY IN MICRODUPLEX Ti-6Al-4V,
     M. Meier and A. K. Mukherjee, <u>Proceedings of Superplasticity in Aerospace II</u>, T. R. McNelley and H. C. Heikkenen, Eds., TMS-AIME, Anaheim, CA pp. 317-332, 1990.

1990

56. THE EFFECT OF ADIABATIC HEATING AND CAVITATION ON THE TENSILE FLOW STABILITY OF HIGH RATE SUPERPLASTICITY, T. R. Bieler and A. K. Mukherjee, Proceedings of Superplasticity in Aerospace II, T. R. McNelley and H. C. Heikkenen, Eds., TMS-AIME, Anaheim, CA pp. 129-141, 1990.

57. HIGH RATE SUPERPLASTIC DEFORMATION MECHANISMS IN IN90211 MECHANICALLY ALLOYED ALUMINUM, T. R. Bieler and A. K. Mukherjee, MRS Meeting, pp. 259-264, 1990.

58. PHENOMENON OF INTERGRANULAR CAVITATION AND FAILURE IN SUPERPLASTICITY, Ho-Sung Lee and A. K. Mukherjee, submitted to Engineering Fracture Mechanics, presented at ICAMP'90 Meeting at UTSONOMIYA, Japan on Aug. 9, 1990.

1991

59. ON THE SUPERPLASTICITY IN SILICON CARBIDE REINFORCED ALUMINUM COMPOSITES, R. S. Mishra and A. K. Mukherjee, Scripta Metall., Vol. 25, pp. 271-275, 1991.

60. α-GRAIN SIZE AND β-VOLUME FRACTION ASPECTS OF THE SUPERPLASTICITY OF Ti-6Al-4V, M. L. Meier, D. L. Lesuer and A. K. Mukherjee, Materials Science and Engineering, Vol. A136, pp. 71-78, 1991.

61. CAVITATION AND FRACTURE OF IN9052 AND IN90211 MECHANICALLY ALLOYED ALUMINUM AT HIGH TEMPERATURE, T. R. Bieler, L. K. Sadilek, S. F. Meagher and A. K. Mukherjee, in Hot Deformation of Aluminum Alloys, edited by T. G. Langdon, et. al., TMS-AIME, pp. 309-318, Warrendale, PA, 1991.

62. DEFORMATION MECHANISMS IN TWO MECHANICALLY ALLOYED ALUMINUM ALLOYS AT HIGH HOMOLOGOUS TEMPERATURES, T. R. Bieler, S. F. Meagher, J. A. Diegel and A. K. Mukherjee, in Hot Deformation of Aluminum Alloys, edited by T. G. Langdon, TMS-AIME, pp.297-260, Warrendale, PA, 1991.

63. THE DEFORMATION AND FRACTURE CHARACTERISTICS OF SUPERPLASTIC ALUMINUM-BASED ALLOYS, A. H. Chokshi and A. K. Mukherjee, in "Hot Deformation of Al Alloys", edited by T. G. Langdon, et. al.,TMS-AIME, pp. 241-260, Pittsburg, PA, 1991.

1992

64. ON SUPERPLASTIC DEFORMATION MECHANISM(S) OF MECHANICALLY ALLOYED ALUMINUM, T. R. Bieler and A. K. Mukherjee, Trans. JIM, Vol. 32, No. 12, pp. 1149-1158, 1992.

1992

65. AN ANALYSIS OF THE SUPERPLASTIC FORMING OF A CIRCULAR SHEET DIAPHRAGM,
H. S. Yang and A. K. Mukherjee, International Journal of Mechanical Sciences, Vol. 34, pp. 283-297, 1992.

66. EFFECT OF COOLING RATE IN OVERAGING AND OTHER THERMOMECHANICAL PROCESS PARAMETERS ON GRAIN REFINEMENT IN AN AA7475 ALUMINUM ALLOY,
H. S. Yang and A. K. Mukherjee, Journal of Materials Science, Vol. 27, pp. 2515-2524, 1992.

67. SUPERPLASTICITY IN A NICKEL SILICIDE ALLOY-MICROSTRUCTURAL AND MECHANICAL CORRELATIONS,
S. L. Stoner, W. C. Oliver and A. K. Mukherjee, Materials Science and Engineering, Vol. A153, pp. 465-469, 1992.

68. THE EFFECTS OF THE α/β PHASE PROPORTION ON THE SUPERPLASTICITY OF Ti-6Al-4V AND IRON-MODIFIED Ti-6Al-4V,
M. Meier, D. Lesuer and A. K. Mukherjee, Materials Science and Engineering, Vol. A154, pp. 165-173, 1992.

69. STRESS REDUCTION TESTS ON Nb-1wt%Zr at 1300K,
M. Biberger, M. J. Davidson and A. K. Mukherjee, Materials Science and Engineering, Vol. A159, pp. 181-185, 1992.

70. CREEP OF NIOBIUM AND SOLID SOLUTION STRENGTHENED Nb-1WT.%Zr,
M.J. Davidson, M. Biberger and A. K. Mukherjee, Scripta Metallurgica et Materialia, Vol. 27, pp. 1829-1834, 1992.

71. COMMENTS ON NORMALIZING THE REDUCED STRAIN RATE FOR STRESS REDUCTION ANALYSIS,
M. J. Davidson and A. K. Mukherjee, Scripta Metallurgica et Materialia, Vol. 27-9, pp. 1201-1204, 1992.

72. EFFECTS OF HYDROSTATIC PRESSURE AND NON-UNIFORM MICROSTRUCTURE ON SUPERPLASTIC FORMING AND POSTFORMED TENSILE PROPERTIES OF AA 7475 ALUMINUM ALLOY,
H. S. Yang, A. K. Mukherjee and W. T. Roberts, Materials Science and Technology, Vol. 8, pp. 611-619, 1992.

73. SUPERPLASTICITY BEHAVIOR OF Ti-6Al-4V AND β-ENHANCED IRON-MODIFIED Ti-6Al-4V,
M. L. Meier and A. K. Mukherjee, Titanium '92, Science and Technology, Vol. II, Symposium Proceedings of the Seventh World Conference on Titanium, Eds. F. H. Froes and I. L. Caplan, pp. 1421-1428, 1992.

1993

74. SUPERPLASTICITY IN METALS, CERAMICS AND INTERMETALLICS,
in Volume 6 in: "Plastic Deformation and Fracture of Materials" volume editor, H. Mughhrabi in the series "Materials Science and Technology" by VCH Verlagsgesellschaft mbH, Germany, pp. 407-460, 1993.

75. COOPERATIVE GRAIN BOUNDARY SLIDING IN MECHANICALLY ALLOYED Al 9021 ALLOY DURING HIGH STRAIN RATE SUPERPLASTICITY,
M. G. Zelin, T. R. Bieler and A. K. Mukherjee, Metallurgical Transactions Communications, 24A, pp. 1208-1212, 1993.

76. THE INFLUENCE OF HYDROSTATIC PRESSURE ON GRAIN BOUNDARY SLIDING IN SUPERPLASTICITY: IMPLICATIONS FOR CAVITATION,
A. Chokshi and A. K. Mukherjee, Materials Science and Engineering, Vol. A171, pp. 47-54, 1993.

1994

77. THE EFFECT OF GRAIN SIZE AND PRESTRAIN ON THE SUPERPLASTIC BEHAVIOR OF 7475 ALUMINUM ALLOY,
M. K. Rao, H. S. Yang and A. K. Mukherjee, Zeitschrift fur Metallkunde, Vol. 85, No. 10, pp. 715-722, 1994.

B-1   IN PRESS

1. SUPERPLASTICITY IN POWDER METALLURGY ALUMINUM ALLOYS AND COMPOSITES,
R. S. Mishra, T. R. Bieler and A. K. Mukherjee, accepted for publication in Acta Metallurgica et Materialia, May, 1994.

2. INSTANTANEOUS STRAIN MEASUREMENTS DURING HIGH-TEMPERATURE STRESS CYCLING OF A DISPERSION-STRENGTHENED NIOBIUM ALLOY,
D. M. Farkas, R. S. Mishra and A. K. Mukherjee, accepted for publication in Scripta Metallurgica et Materialia, December, 1994.

B-2   SUBMITTED

1. THRESHOLD STRESS MEASUREMENT OF A DISPERSION-STRENGTHENED Nb-1wt%Zr-0.1wt%C ALLOY,
D. M. Farkas and A. K. Mukherjee, submitted to Materials Science and Engineering, November, 1994.

29

IN PREPARATION

1. MICROSTRUCTURE AND CREEP BEHAVIOR OF A Nb-1wt%Zr-0.1wt%C ALLOY,
   D. M. Farkas and A. K. Mukherjee

2. INTERNAL STRESS MEASUREMENTS OF A Nb-1wt%Zr-0.1wt%C ALLOY,
   D. M. Farkas and A. K. Mukherjee

3. THERMODYNAMICS ANALYSIS OF CARBIDE FORMATION IN A Nb-1wt%Zr-01wt%C ALLOY,
   D. M. Farkas, A. K. Mukherjee and J. R. Groza

Appendix A - Details of the manufacturing process and heat treatments

EXTRUSION

Ingot Approx 8 inches diameter, 25 inches long was EDM machined to remove the inner 3.25 in to form a tube shell. Shell was canned in niobium to preclude oxidation during the extrusion process. The canning was performed by NRC of Boston MA. The shell was then extruded at 1860 K to a 8/1 ratio resulting in a tubular shell approximately 200 inches long.
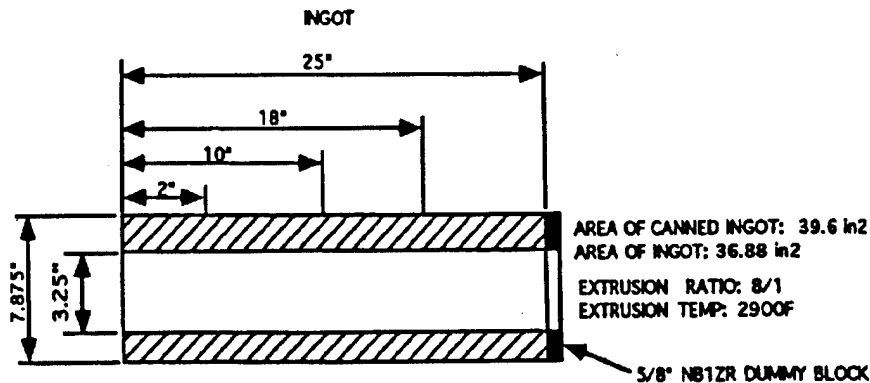
Oxygen contamination tests performed by General Electric Aerospace Division following extrusion are listed below:

Tube shell section	O2 result (ppm)	
T1 front 60 inches of shell	98-271	234 mean
T2 mid 60 inches of shell	301-327	314 mean
T3 back end 60 inches of shell	131-185	158 mean*

*Only the back end section (T3) was used in the final comercial application. The majority of the creep specimens were fabricated from this section. Several specimens were provided from the front end to investigate variation in mechanical properties.

Appendix A - Details of the manufacturing process and heat treatments

TUBE FABRICATION (COLD WORK) AND ANNEAL

Extruded ingot cut to 3.85" OD, 0.31" wall thickness and sectioned.

Roll to 0.150" thick (50% CW)

Roll to 0.030" thick (91% CW)

Machine tensile specimen per drawing

Final anneal; 1 hr 1855 K + 2 hr 1477 K for target grain size of 50 - 90 microns

Final anneal; 1 hr 1755 K + 2 hr 1477 K for target grain size of 10 - 40 microns
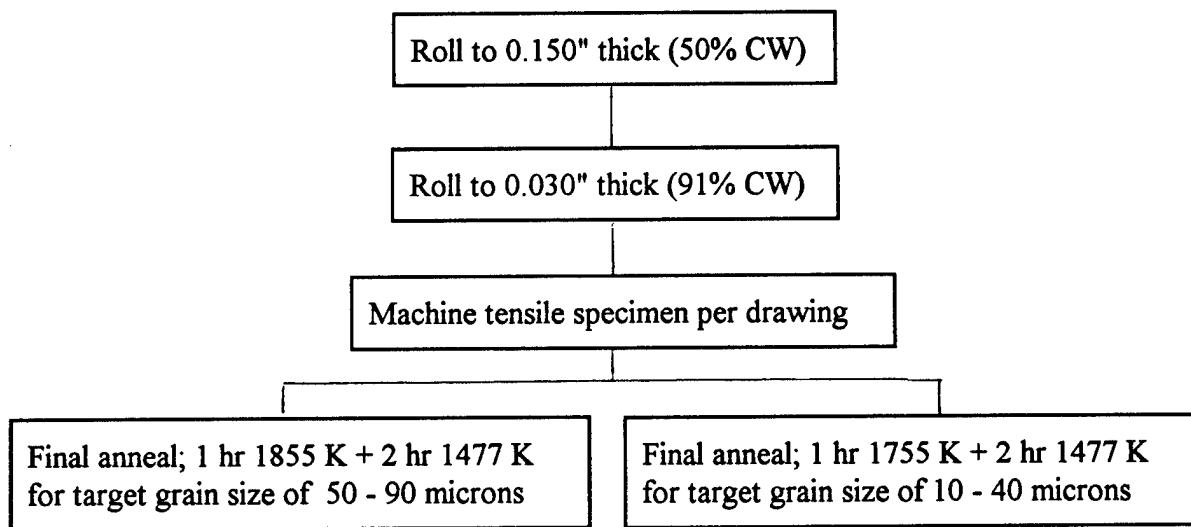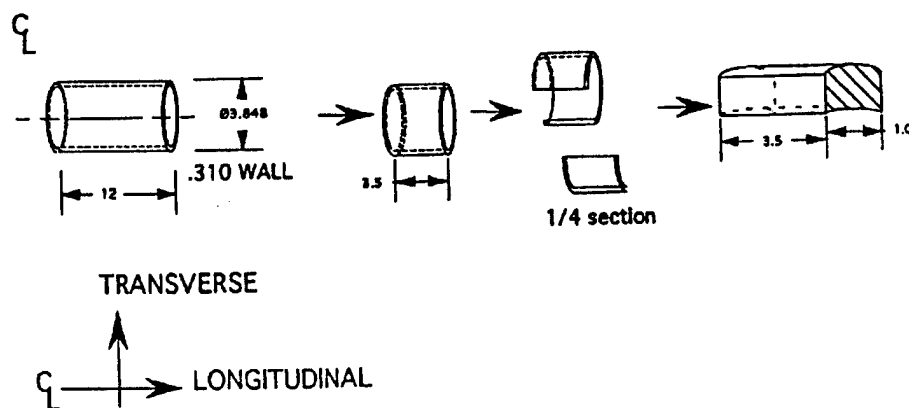
Appendix B Statistical Distribution of Particle Spacing

This appendix details the calculations used to determine the Orowan bowing stress based on a statistical distribution of particles in a dispersion-strengthened matrix. The following definitions are used throughout.

r	particle radius
r_s	particle radius of slice on a dislocation glide plane
$\overline{r_s}$	mean radius of a single particle cross-section for all glide plane slices
$\overline{\overline{r_s}}$	mean radius of a distribution of particle cross-sections for all glide plane slices
$\overline{r}$	mean particle radius of the distribution
$\overline{r^2}$	mean of the square of the radii of the distribution
$\overline{r^3}$	mean of the cube of the radii of the distribution
f	volume fraction of particles
$\overline{\lambda}$	mean distance between particle surfaces on a dislocation glide plane
T_s	mean center-to-center distance between particles of the distribution
N_v	volume density of particles (no. of particles per unit volume in matrix)
N_s	planar density of particles (no. of particles per unit area on a plane)
$n(r)$	particle size distribution function
$F(r)$	frequency function of particle distribution

1.   Particle size distribution

For a given sampling of particles, each of different radius r, the size distribution is obtained as shown in Fig. B1 by measuring each particle and tabulating the amount of particles of each size.

Particle Radius r (μm)
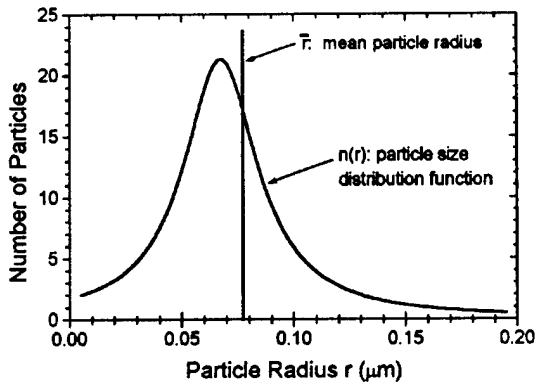
The mean of the distribution (also called the expectation or weighted average) is found from:

$$\overline{r} = \frac{\sum r}{N_v} \qquad \text{(B1)}$$

where in this case the volume density N_v is the number of particles in the sample unit volume. The function (or curve) which describes the size distribution is n(r) and is defined such that the area under the distribution curve equals the volume density (total number of particles in the sample volume). Thus the area under the particle size distribution function represents N_v via the relation:

$$N_v = \int_0^\infty n(r)\,dr \qquad \text{(B2)}$$

33

Appendix B   Statistical Distribution of Particle Spacing

A more appropriate way of describing a sampling of particle sizes is to normalize the distribution function by the volume density N_v such that the appearance of the distribution is independent of the sampling size as shown in Fig. B2.
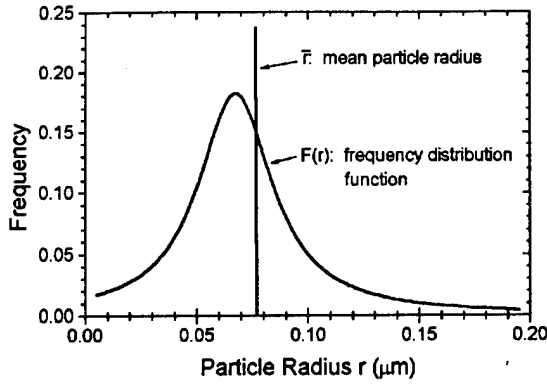
This normalization becomes the frequency function F(r) (or the probability of a particle having a given radius r) of the distribution of particle radii (r) defined by:

$$F(r) = \frac{n(r)}{N_v} \qquad \text{(B3)}$$

It is to be noted that now the total area under the frequency function equals 1. This also facilitates a more appropriate definition of mean particle radius. From statistics, the expectation (or expected value or mean) of a random variable is a weighted average of the values of the selected parameter, where each value of the parameter is weighted by its probability of occurrence. The mean particle radius $\bar{r}$ is thus defined as:

$$\bar{r} = \int_0^\infty r \cdot F(r)dr \qquad \text{(B4)}$$

The mean of the square and cube of the distribution of particle radii are defined in a similar manner and are easily computed from the statistical capabilities of a spread sheet program.

2.   Mean center-to-center spacing $\bar{l}_s$

Figure B3 illustrates the approach to finding the mean center-to-center distance between particles of the distribution. Shown at right are two particles of arbitrary size cut by a dislocation glide plane. Dimensional definitions are as shown.

Fig. B3. Diagram of particles on glide plane.
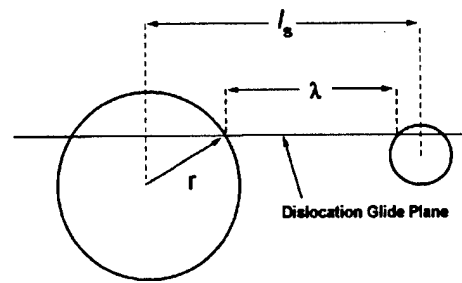
The planar density N_s is defined as the number of particles per unit area on a given dislocation glide plane:

$$N_s = \int_0^\infty 2r \cdot N_v F(r)dr = 2\bar{r}N_v \qquad \text{(B5)}$$

34

Appendix B   Statistical Distribution of Particle Spacing

If a simple square arrangement is assumed, the mean center-to-center distance between particles is simply the inverse of the square root of the planar density given by:

$$\bar{l}_s = \frac{1}{\sqrt{N_s}} \tag{B6}$$

For a more random arrangement of "strong" obstacles, the mean center-to-center distance between particles is multiplied by a factor of 1.25 [B1]:

$$\bar{l}_s = \frac{1.25}{\sqrt{N_s}} \tag{B7}$$

Substituting for N_s yields the expression:

$$\bar{l}_s = \frac{1.25}{\sqrt{2\bar{r}N_v}} \tag{B8}$$

In a similar way, the volume fraction f of a distribution of particles is found by:

$$f = \int_0^\infty \frac{4}{3}\pi r^{3} N_v F(r)dr = \frac{4}{3}\pi N_v \bar{r}^{3} \tag{B9}$$

This expression is solved for N_v in terms of f and $\bar{r}^3$ and substituted into expression (B8) to yield the desired form of the mean center-to-center spacing:

$$\bar{l}_s = 1.25 \sqrt{\frac{2\pi\bar{r}^{3}}{3 f \bar{r}}} \tag{B10}$$

3.   Slip plane intersection with particles
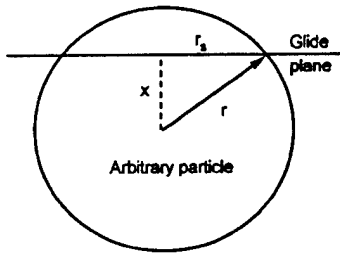
Fig. B4. Particle on slip plane.

In addition to consideration for the distribution of particle sizes, the location of where a particular slip plane cuts through the particles must be accounted for when determining the mean particle surface-to-surface separation distance $\bar{\lambda}$. Figure B4 shows a selected particle cut by an arbitrary slip plane. The mean radius of a single particle cross-section for all glide plane slices $\bar{r}_s$ is given by:

$$\bar{r}_s = \frac{1}{r}\int_0^r r_s dx \tag{B11}$$

35

Appendix B   Statistical Distribution of Particle Spacing

It can be seen however, that r_s is a function of the particle radius by the relation:

$$r_s = \sqrt{r^2 - x^2} \tag{B12}$$

Substituting this expression for r_s into equation (B11) and evaluating the integral yields:

$$\bar{r}_s = \frac{1}{r}\int_0^r \sqrt{r^2 - x^2}\,dx = \frac{\pi r^2}{4} \tag{B13}$$

For a distribution of particle radii, the mean of the mean radii of a all particle cross-sections (in effect, a double mean), $\bar{\bar{r}}_s$ is given by:

$$\bar{\bar{r}}_s = \frac{1}{N_s}\int_0^\infty \bar{r}_s\,dN_s \tag{B14}$$

Again substituting the evaluated expression for $\bar{r}_s$ from equation (B13) and N_s from equation (B5) yields the desired expression for the mean radius of a distribution of particle cross-sections for all glide plane slices:

$$\bar{\bar{r}}_s = \frac{1}{2\bar{r}N_v}\int_0^\infty \frac{\pi r}{4}\cdot 2rN_v F(r)\,dr = \frac{\pi \bar{r}^2}{4\bar{r}} \tag{B15}$$

The final expression for mean particle separation on an arbitrary glide plane is obtained from:

$$\bar{\lambda} = \bar{l}_s - 2\bar{\bar{r}}_s \tag{B16}$$

Thus:

$$\bar{\lambda} = 1.25\sqrt{\frac{2\pi \bar{r}^3}{3f\,\bar{r}}} - \frac{\pi \bar{r}^2}{2\bar{r}} \tag{B17}$$

Reference
B1. A.J.E. Foreman and M.J. Makin, Phil. Mag. 14, p. 911 (1966)

Appendix C Instantaneous Strain Measurements During High-Temperature Stress Cycling
of a Dispersion-Strengthened Niobium Alloy

Introduction

Stress cycling tests have been used extensively to interrogate and interpret the mechanisms
of high-temperature creep of materials. Various researchers have used these techniques to
determine such parameters as internal back stress [1,2,3,4], instantaneous strain [2,5,6], work-
hardening rate [2,7], the shape of creep transient, and have used such experiments to classify the
type of creep behavior [6]. Measurements from stress change tests during steady-state creep have
shown that the total instantaneous strain measured for stress changes exceeded the values
calculated from elastic behavior alone. Additionally, previous researchers have found that the
total instantaneous strain resulting from a stress addition was typically greater than the total
instantaneous strain resulting from a stress reduction [2,5,6].

Traditionally, stress changes have been performed during steady state creep (constant
structure) to determine the back stress component of the applied stress. More recently, a
modified stress reduction technique has been used to determine the internal stress throughout the
strain history (primary, steady-state and tertiary components of creep) of alloy and particle
strengthened materials [4].

This presentation reports new results of stress cycling tests performed on a dispersion
strengthened niobium alloy during high-temperature creep using methods described by Pahutova,
et al [4]. The measured instantaneous strain resulting from each stress change is used to describe
the work-hardening behavior of this alloy with accumulated strain. Some correlations to the
dislocation link-length distributions and dislocation mobility under changing stress conditions are
made.

Experimental

Creep specimens of Nb-1wt%Zr-0.1wt%C (PWC-11) were obtained with an "industry
standard thermomechanical processing treatment" consisting of an extrusion at 1873 K, cold work
of approximately 90%, followed by a final two-part anneal of 1 hr at 1755 K + 2 hr at 1477 K.
Samples were tested at 1434 K ($\sim$0.5 T_m) under vacuum of 2 x 10^{-6} torr or better using a
constant-stress creep machine. The stress level was cycled between the upper value of 53.5 MPa
and a given lower value depending on the desired percentage of stress reduction. Reduced stress
levels used were 49.2 MPa (8% reduction), 46.8 MPa, (13% reduction) and 36.3 MPa (32%
reduction). Stress changes were performed by manually removing (or adding) a stack of weights
from the load platform of the constant stress creep machine. The same weight stack was removed
(or added) for a given stress change set for the duration of the test; the Andrade-Chalmers lever
arm compensating for strain to maintain the desired constant stress and magnitude of stress
change. Strain was measured using a super-linear variable capacitor (SLVC) input to a HP-
3457A digital multimeter and fed to a PC computer via a IEEE-488.2 GPIB interface. An overall
strain resolution of 2 x 10^{-7} was achieved. During stress cycling, a high-speed data acquisition
mode was selected allowing stress and strain to be recorded every 0.1 seconds. A total of 30 to
40 complete stress cycles were made resulting in an accumulated strain of about 0.25 for each set.
(Here we define a set as the data acquired for all stress cycles from the upper value to a single
value of reduced stress.)

Appendix C   Instantaneous Strain Measurements During High-Temperature Stress Cycling
of a Dispersion-Strengthened Niobium Alloy

Results

Figure 1 presents a comparison of the strain rate immediately preceding each stress
reduction (for one of the data sets) with that produced from a monotonic creep test at the same
stress and temperature. This comparison clearly indicates that the act of stress cycling itself did
not introduce any significant effect in the creep (work-hardening or recovery) behavior of this
alloy. It should also be noted that steady-state strain rate for the monotonic creep test is reached
after approximately 5% strain ($\epsilon = 0.05$).

The creep behavior observed for each set of stress cycles was of the normal type, ie., an
instantaneous strain jump followed by decreasing strain rate with time for a stress addition and an
instantaneous strain drop followed by either a reduced strain rate or an anelastic transient for a
stress reduction. Such behavior is typical for both pure metals and class II creep alloys. The
instantaneous strain obtained during the stress transient is composed of an elastic portion and a
(instantaneous) plastic portion:

$$\Delta \epsilon^{instantaneous} = \Delta \epsilon_{(elastic)} + \Delta \epsilon^{instantaneous}_{(plastic)} \tag{1}$$

Figure 2 shows selected strain data obtained (using the high-speed acquisition mode) for the three
sets of stress reductions at different values of accumulated strain. The instantaneous strains
measured during stress reductions all typically occurred within 0.1 seconds and were easy to
distinguish from any follow-on anelastic behavior. A marked difference can be seen in the
magnitude of instantaneous strains for a given stress reduction level for increasing values of
accumulated strain.

Figure 3 plots instantaneous strains for all stress changes with accumulated strain. The
general instantaneous strain response can be summarized in the following points:
1. The instantaneous strains from the stress additions were typically larger than the
   instantaneous strains for the stress reduction near the same approximate accumulated
   strain value.
2. The total instantaneous strain decreased with accumulated strain even though the
   magnitude of the stress change was held constant for a given set. This effect has not
   been reported in previous literature.
3. The difference between the instantaneous strains from a stress addition and a stress
   reduction for a given $\Delta \sigma$ decreases as $\Delta \sigma$ increases.
Also shown on Fig. 3 are the expected values of the elastic strain for the change in stress
calculated from the elastic modulus of pure niobium at the test temperature (100 GPa)[8].

Discussion

As stated in point 1 above, the general trend was that a stress addition produced more
instantaneous strain change than a stress reduction. This effect has been reported in literature
[2,5,6]. It should be noted that in some cases (mostly during the larger $\Delta \sigma$ sets), the
instantaneous strain from a given stress addition was actually less than that for a stress reduction.
This effect may have resulted from the difficulty to measure the transient accurately because the

38

Appendix C   Instantaneous Strain Measurements During High-Temperature Stress Cycling
of a Dispersion-Strengthened Niobium Alloy

recorded stress change was not so abrupt (occurring over approximately 1 second). We believe
this to be partly do to the inertia of the load train and the operator's ability to add the large weight
stack while avoiding oscillations in the creep machine's load train. Even so, it can be seen that
the instantaneous plastic portion decreases with accumulated strain and becomes fairly constant
after about 0.10 to 0.15 strain, well after steady state creep typically occurs for this material under
similar (constant) stress and temperature conditions.

The production of instantaneous plastic strain on a stress addition can be attributed to the
change in threshold dislocation link length λ_{th} assuming a three-dimensional dislocation network
with a typical distribution function $\phi(\lambda,t)$ [6,9,10,11]. The threshold link length is a unique
function of the applied stress for a given material:

$$\lambda_{th} = \alpha \frac{Gb}{\tau_a} \tag{2}$$

where G is the shear modulus, b the Burger's vector, τ_a the applies shear stress, and α a constant
which relates the strength of the obstacle. In the present alloy, the dislocation network has a
combination of pinning elements which includes both particles and forrest dislocations [12]. The
threshold link length is reduced by the amount $\Delta\lambda$ for a given stress addition $\Delta\tau$ by:

$$\Delta\lambda = \lambda_{th}\frac{\Delta\tau}{\tau_a} \tag{3}$$

Those dislocation links of length λ_{th} to $\lambda_{th} - \Delta\lambda$ which were initially immobile at the lower stress
burst forward from their pinning points during the stress addition resulting in a net
"instantaneous" plastic strain. A minor additional instantaneous plastic strain results from the
increased area swept by "bowed out" segments of pinned dislocations aligned favorably in the slip
plane. A stress reduction however, increases the threshold dislocation link length and the only
instantaneous plastic strain which results arises from the area swept back of pinned segments
relaxing under the influence of reduced line tension. Thus it is expected that the instantaneous
strain from a stress addition would be larger than that from a corresponding stress reduction
unless the magnitude of $\Delta\sigma$ exceeds the measured internal stress. In the present case, the
measured internal stress under the imposed applied stress and temperature is approximately 85 to
90% of the applied stress [13]. This may explain why the difference in instantaneous plastic strain
between a stress addition and a stress reduction diminishes with increased $\Delta\sigma$. Stress reductions
greater than the internal stress allow the release of pinned dislocation segments in the reverse
direction. It should be noted that several of the recorded instantaneous strains were less than the
calculated elastic strains using the modulus for pure niobium at the test temperature. This was
especially pronounced for large stress additions at large accumulated strains. Pending a more
accurate measurement of this alloy's modulus, this effect as yet, cannot be accounted for.

The measured instantaneous strains can be exploited to determine the apparent work
hardening rate H which is calculated from the expression [2]:

39

Appendix C   Instantaneous Strain Measurements During High-Temperature Stress Cycling of a Dispersion-Strengthened Niobium Alloy

$$\Delta H = \frac{\Delta \sigma}{\Delta \epsilon^{instantaneous}_{(plastic)}} \qquad (4)$$

The instantaneous plastic strain is usually found by subtracting the elastic portion from the total measured instantaneous strain resulting from a stress addition. The true work hardening rate h, is then determined by extrapolating the plot of log H versus $\Delta \sigma$ as $\Delta \sigma \rightarrow 0$. In the present case, the value of the instantaneous plastic strain change used in equation (4) was determined from [2]:

$$\Delta \epsilon_p = \Delta \epsilon_+ - \Delta \epsilon_- \qquad (5)$$

where $\Delta \epsilon_+$ is the instantaneous strain change from the stress addition and $\Delta \epsilon_-$ is the instantaneous strain change from the stress reduction. This method was employed due to the observation that some of the measured instantaneous strains were less than the calculated elastic strain based on the modulus of pure niobium. Figure 4 shows the plot of instantaneous plastic strain change as calculated by equation (5) versus accumulated strain for the 13% stress change set. Even though significant data scatter is present, the least-square-error line reveals that the plastic strain change remains fairly constant after about 0.05 accumulated strain. This corresponds roughly to the strain value where steady-state strain rate is reached in the monotonic creep test shown in Fig. 1. The true work hardening rate, h, is estimated from [2]:

$$h = \lim H \quad as \quad \Delta \sigma \rightarrow 0 \qquad (6)$$

Figure 5 plots log H versus $\Delta \sigma$ for the values of H determined from Fig 4. Extrapolating the line to zero $\Delta \sigma$ reveals the true work hardening rate h $\approx$ 7 GPa. When expressed as a fraction of the elastic modulus (E = 100 GPa for pure Nb at test temperature), h/E $\approx$ .07. It should be pointed out that although the instantaneous strains decreased with accumulated strain, the true work-hardening rate remained fairly constant which would be expected under steady state creep conditions.

Conclusions

Experimental results obtained from stress cycling tests performed during high-temperature creep of a dispersion strengthened niobium alloy indicate that the instantaneous strain following the stress change decreases with accumulated strain. The true work-hardening rate was shown to be a small fraction of the elastic modulus which remained fairly constant throughout the strain history. The instantaneous strain change from a stress addition was typically greater than the strain from the corresponding stress reduction. This effect is quite pronounced for small stress changes and diminishes as the magnitude of the stress change increases. This implies that the mobility of dislocations is impeded in the reverse direction unless the magnitude of stress reduction exceeds the value of the internal stress.

Appendix C   Instantaneous Strain Measurements During High-Temperature Stress Cycling
of a Dispersion-Strengthened Niobium Alloy

References

1. Poirier, J.P., "Microscopic Creep Models and the Interpretation of Stress-Drop Tests During
    Creep", Acta Metallurgica, Vol 25, pp. 913-917, 1977.
2. Northwood, D. O. and Smith, I.O., "Steady-State Creep and Strain Transients for Stress
    Change Tests in an Al-0.5wt%Zn Solid Solution Alloy", Phys. Stat. Sol. (a) 115, 125 (1989).
3. Burton, B., "Internal stresses, stress change tests and the formulation of recovery creep
    equation", Philosophical Magazine Letters, 1990, Vol. 62, No. 6., 383-388.
4. Pahutova', M., Dlouhy', A. and Cadek, J., "An Experimental Method to Estimate Internal
    Stress Level During High Temperature Creep", Scripta Metallurgica et Materialia, Vol 29,
    1993, pp. 599-604.
5. Langdon, T.G. and Yavari, P., "The Effect of Instantaneous Strain on Creep Measurements
    at Apparent Constant Structure", Creep and Fracture of Engineering Materials and
    Structures, Proceedings of the International Conference, Swansea, 1981, pp 71-84.
6. Shi, L., and Northwood, D.O., "Instantaneous Strains in Stress Change Tests During Steady-
    State Creep", Creep and Fracture of Engineering Materials and Structures, Proceedings of
    the Fifth International Conference, Swansea, 1993, pp 11-20.
7. Ajaja, O., "The Stress Change Technique of Determining Work-Hardening Rates During
    Creep:, Acta metall. mater. Vol. 40, No. 10, pp 2701-2706, 1992.
8. Niobium, Proceedings of Int. Symposium, ed. H. Stuart, TMS, (1984).
9. Ajaja, O., "Role of recovery in high temperature constant strain rate deformation", Journal of
    Materials Science, 26 (1991), pp. 6599-6605.
10. Shi, L. and Northwood, D.O., "On Dislocation Link Length Statistics for Plastic
    Deformation of Crystals", phys. stat. sol. (a) 137, 75 (1993), pp 75-85.
11. Lagneborg, R., Forsen, B.H., Wiberg, J., "A Recovery-Creep Model Based Upon
    Dislocation Distributions", Proceedings of Creep Strength in Steel and High Temperature
    Alloys, TMS, (1974), pp 1-7.
12. Farkas, D.M., Mishra, R.S., and Mukherjee, A.K., "Microstructure and Creep Behavior of a
    Nb-1wt%Zr-0.1wt%C Alloy", to be published.
13. Farkas, D.M., Mishra, R.S., and Mukherjee, A.K., "Internal Stress Measurement of a Nb-
    1wt%Zr-0.1wt%C Alloy", to be published.
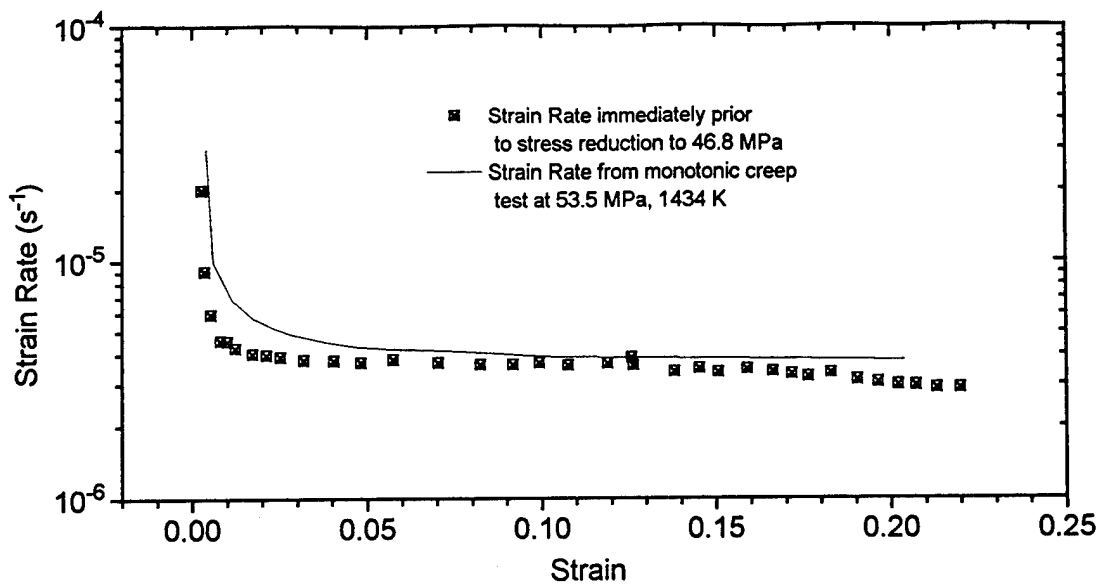
Figure 1. Comparison of strain rate behavior from stress cycling test and monotonic creep test at 53.5 MPa and 1434 K.
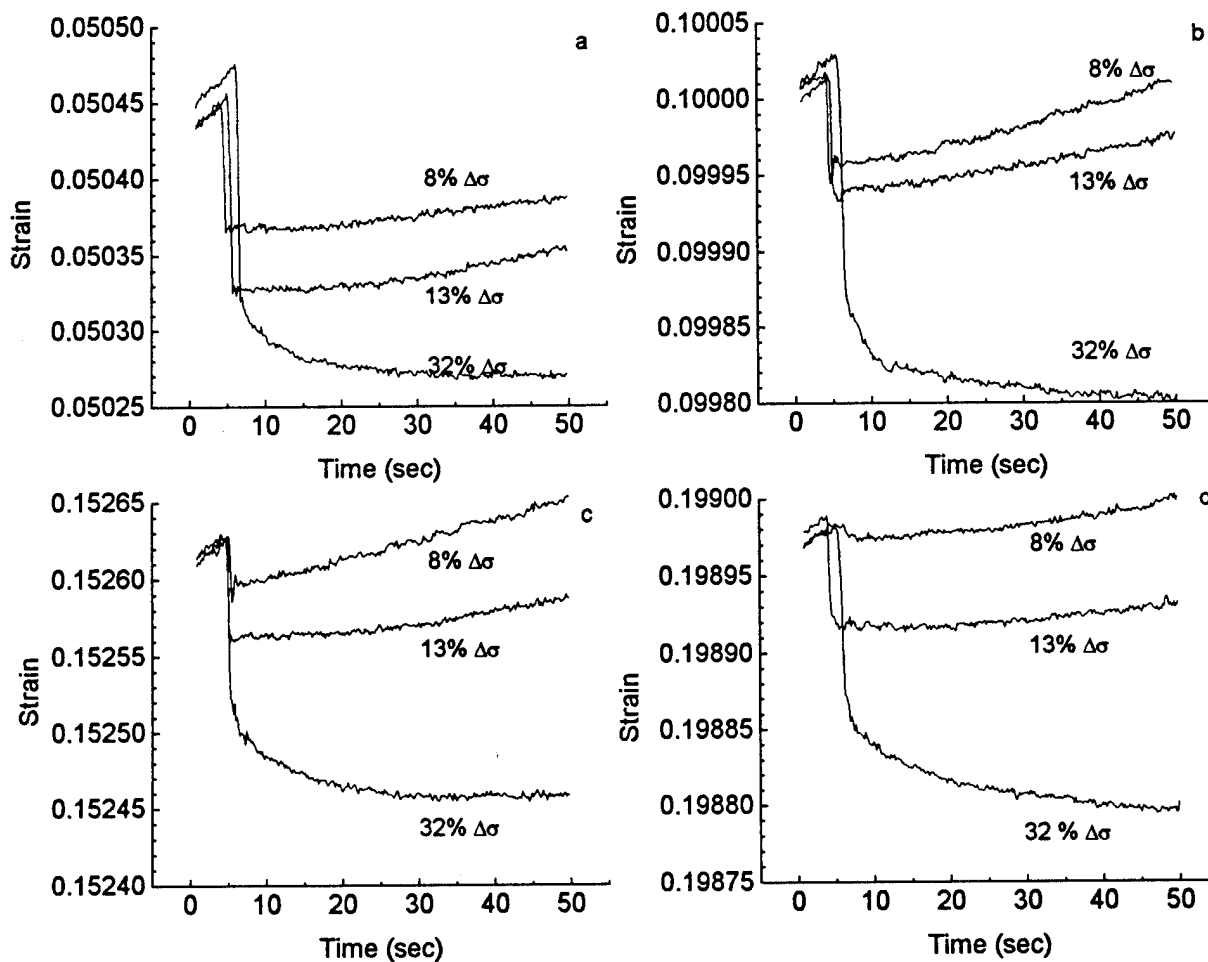
Figure 2. Strain behavior versus time for three levels of stress reductions: (a) at 5% accumulated strain, (b) at 10% accumulated strain, (c) at 15% accumulated strain, (d) at 20% accumulated strain.
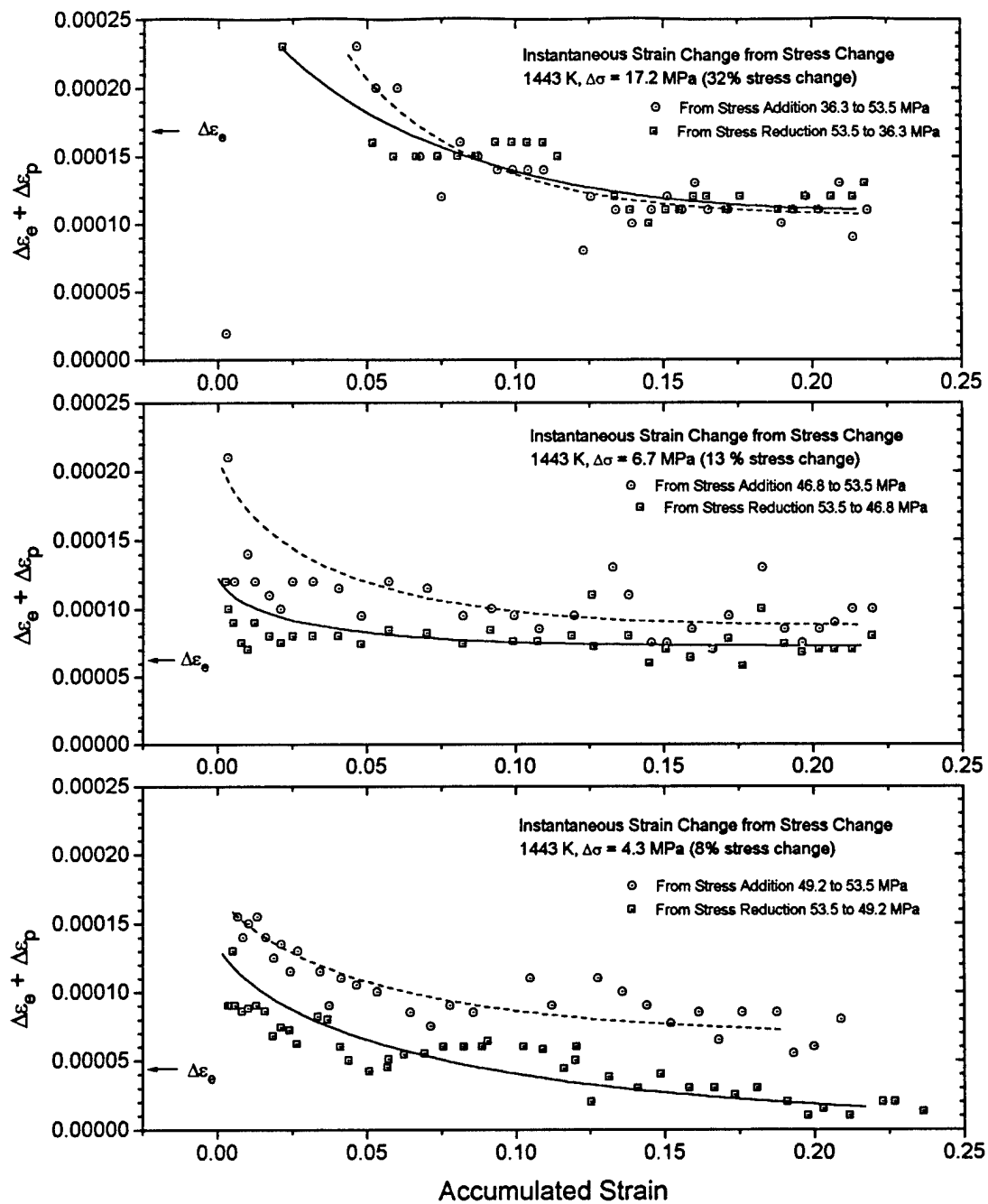
Figure 3. Instantaneous strains measured during stress cycling.
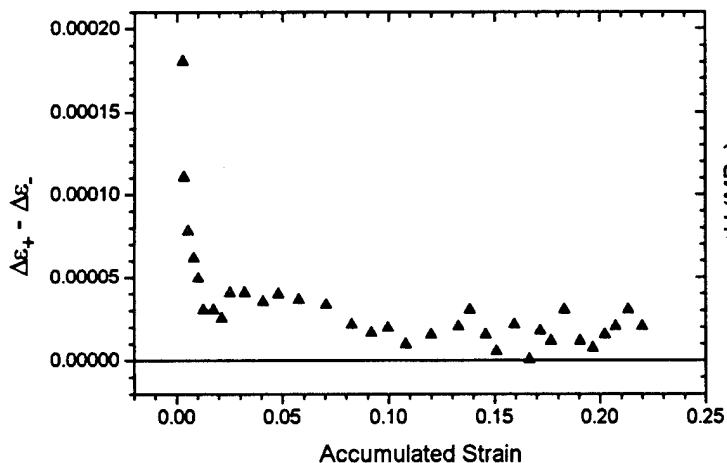
Figure 4. Instantaneous plastic strain difference versus accumulated strain for 13% stress change.
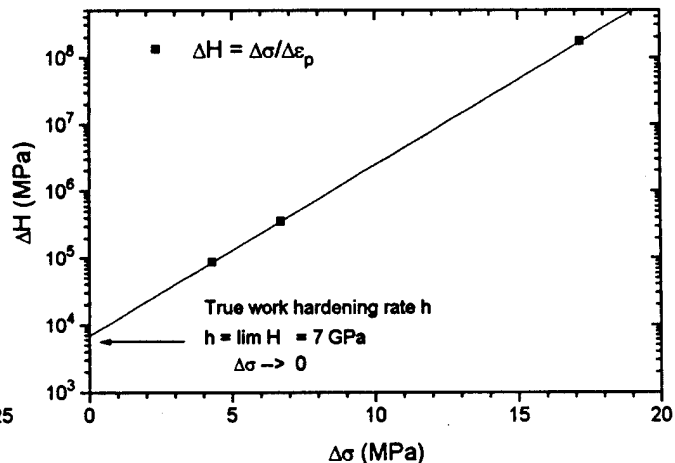
Figure 5. Log H versus $\Delta\sigma$ extrapolated to $\Delta\sigma = 0$ to obtain true work hardening rate h.

43
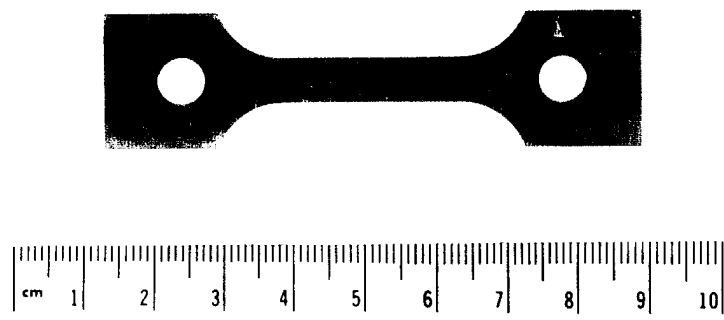
Figure 1. Typical creep test specimen of Nb-1wt%Zr-0.1wt%C
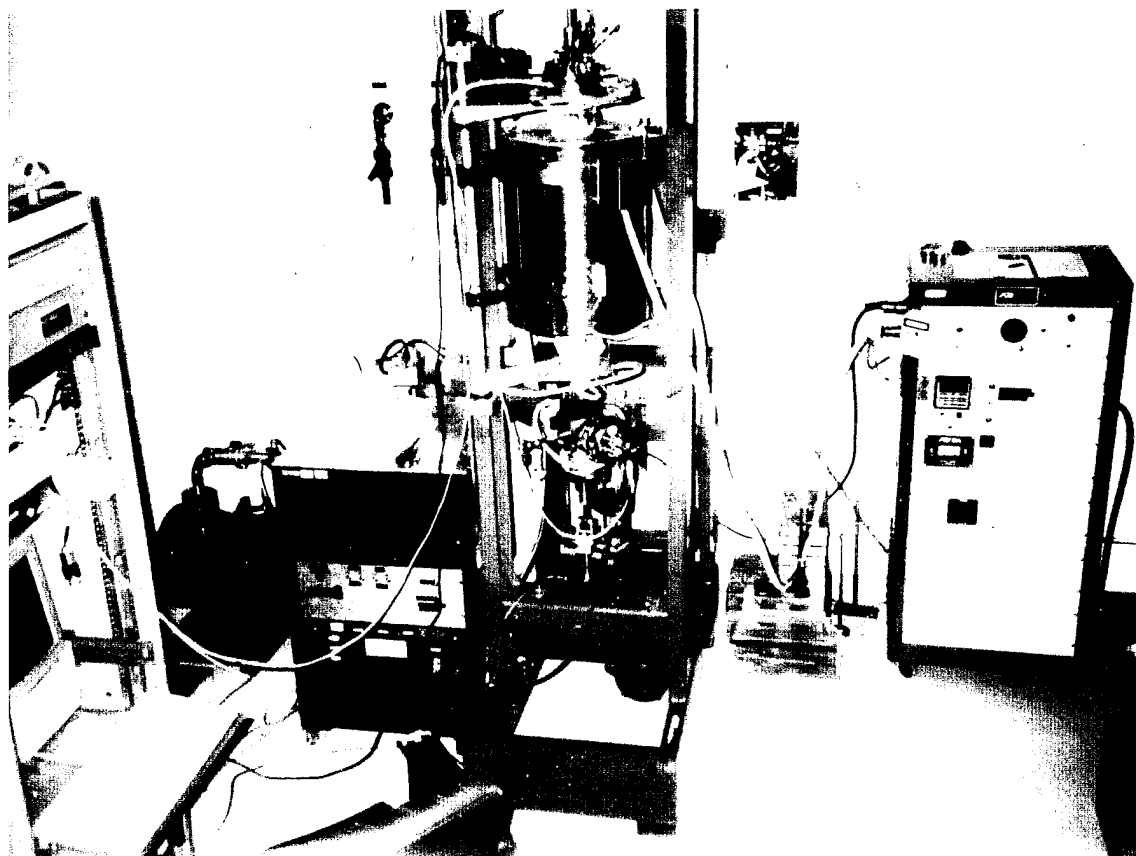
Figure 2. Complete creep test apparatus showing retort and furnace in center.
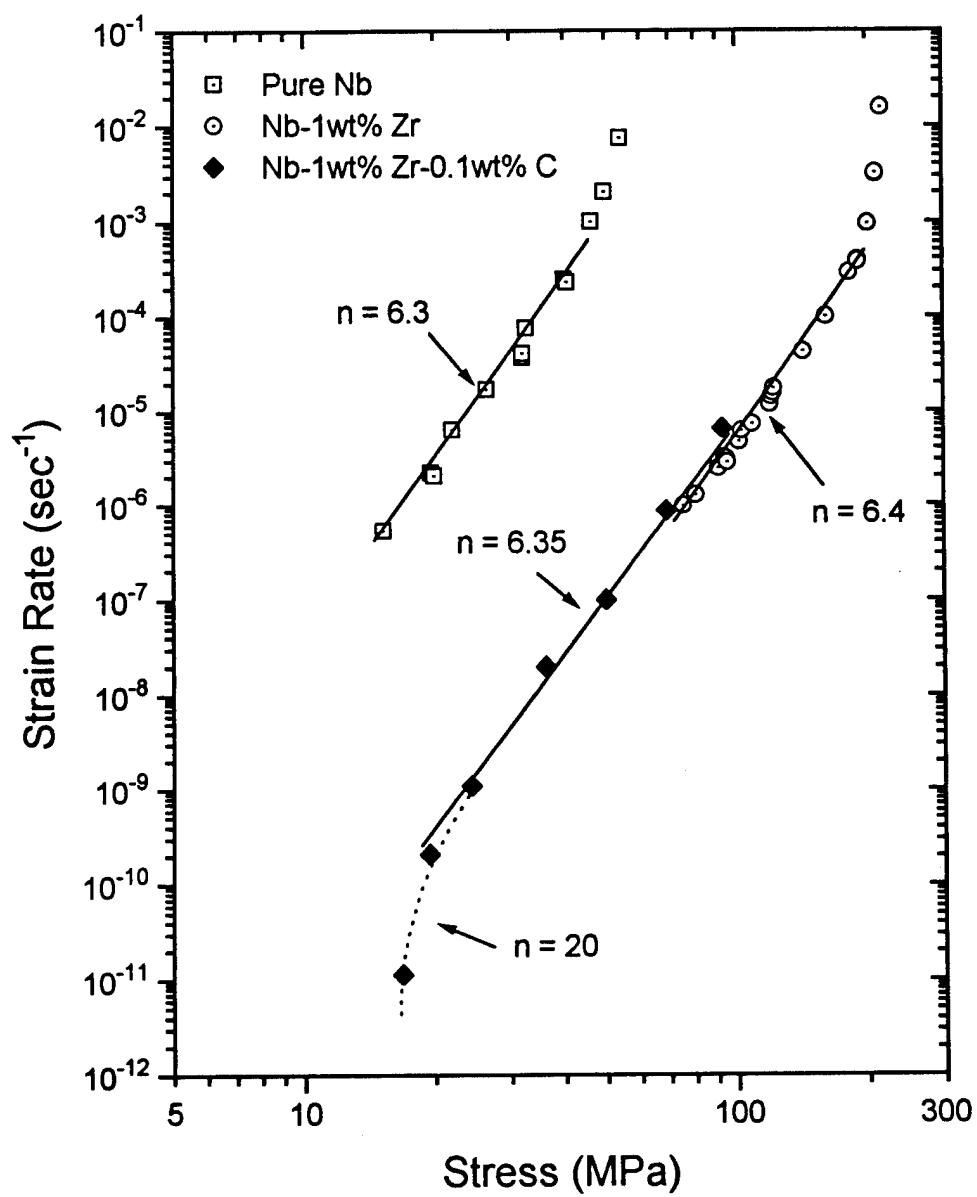
Figure 3. Steady state creep behavior of niobium alloys
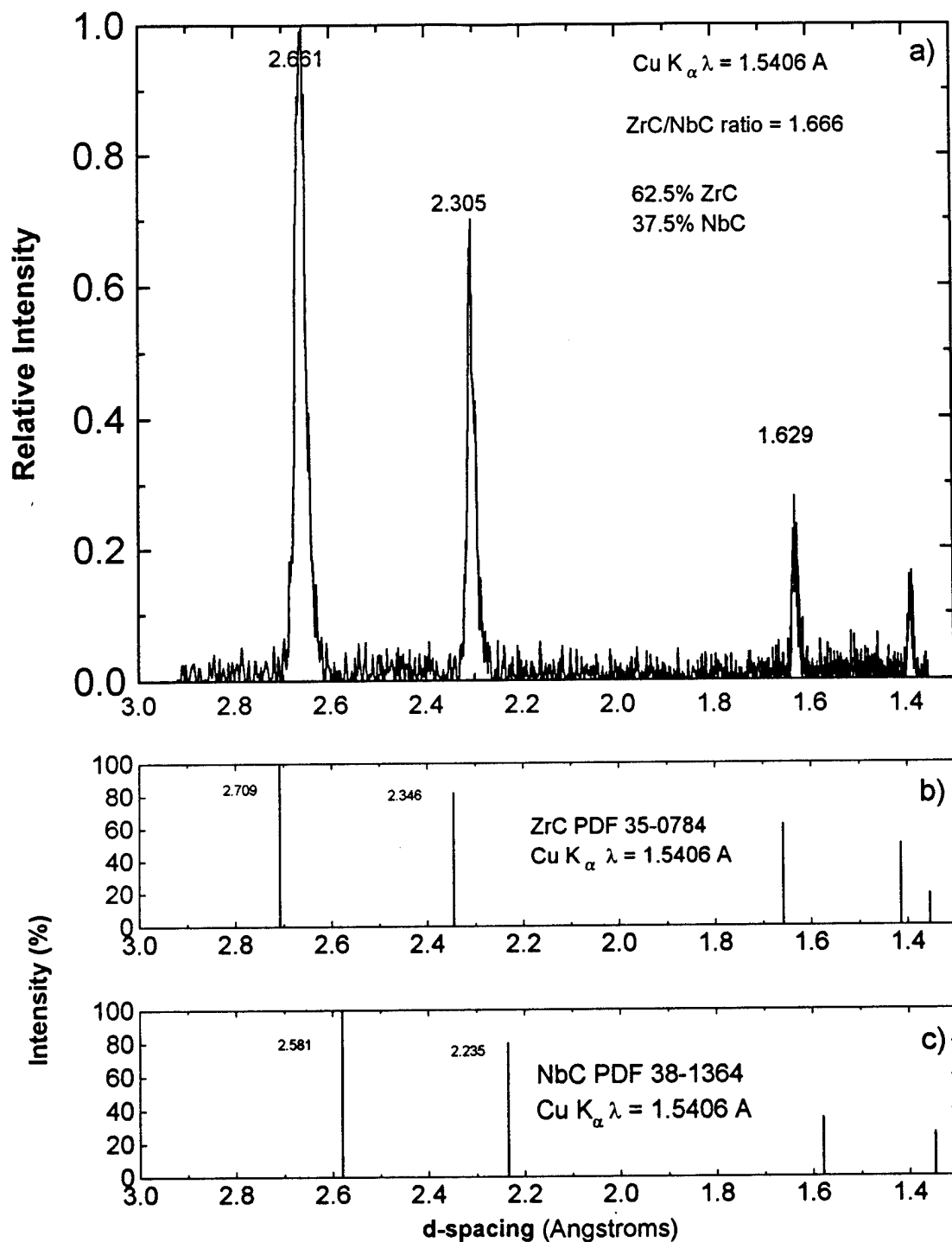
Figure 4. a) X-ray spectrum from extracted carbide particles of as-received Nb-1wt%Zr-0.1wt%C alloy. Powder diffraction spectrums for b) ZrC and c) NbC. Calculated carbide lattice parameter = 0.461 nm
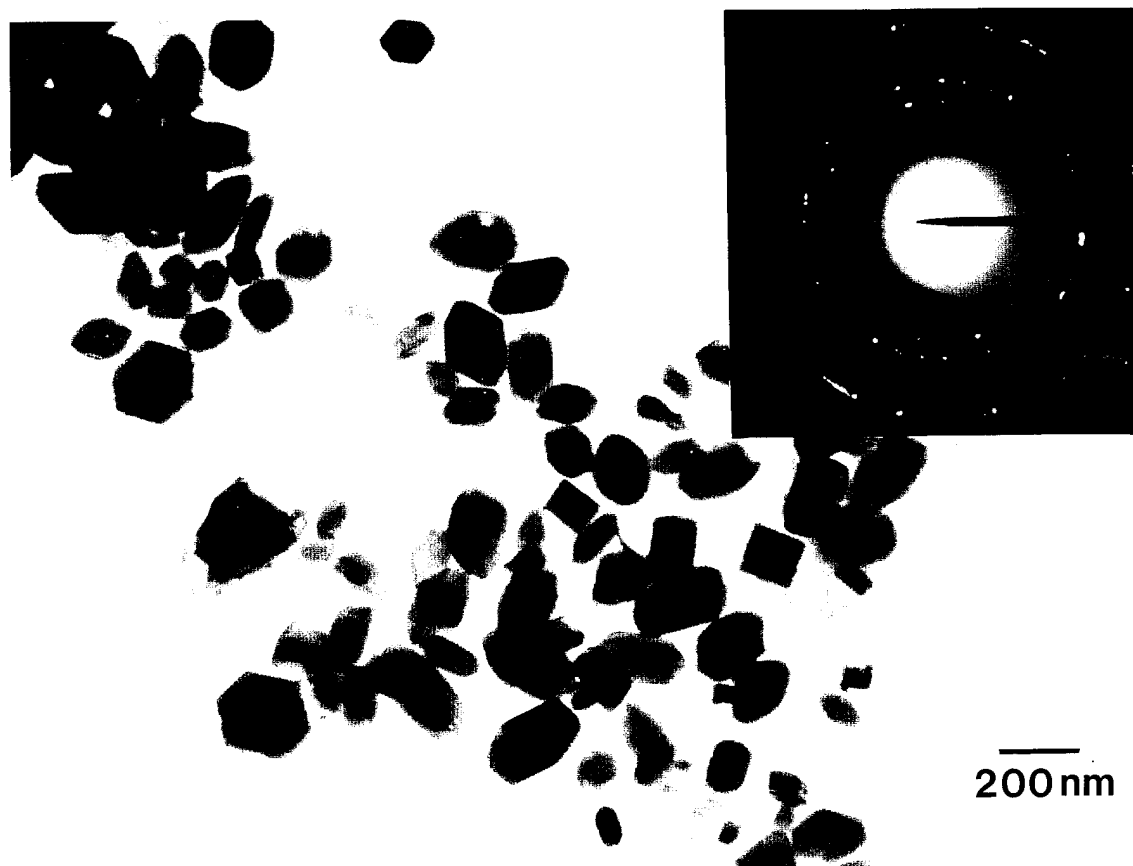
Figure 5. TEM micrograph of extracted (Nb,Zr)C carbide particles from as-received
alloy. Magnification of negative 27.5 kX. Size marker shown.
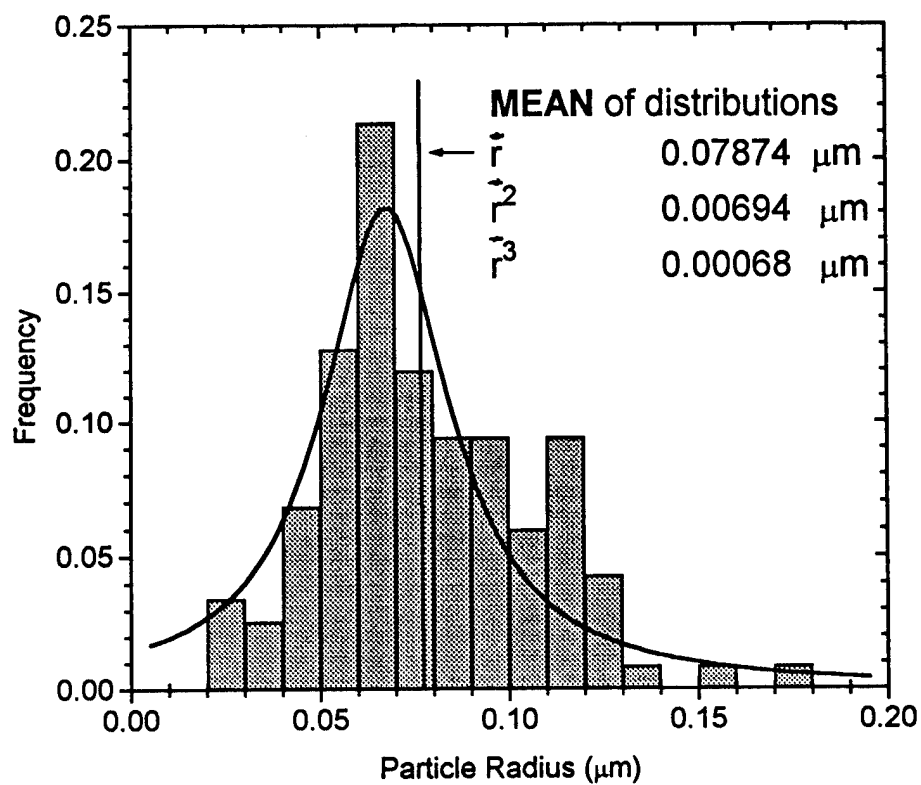
Figure 6. Size distribution histogram of extracted carbide particles from as-received Nb-1wt%Zr-0.1wt%C
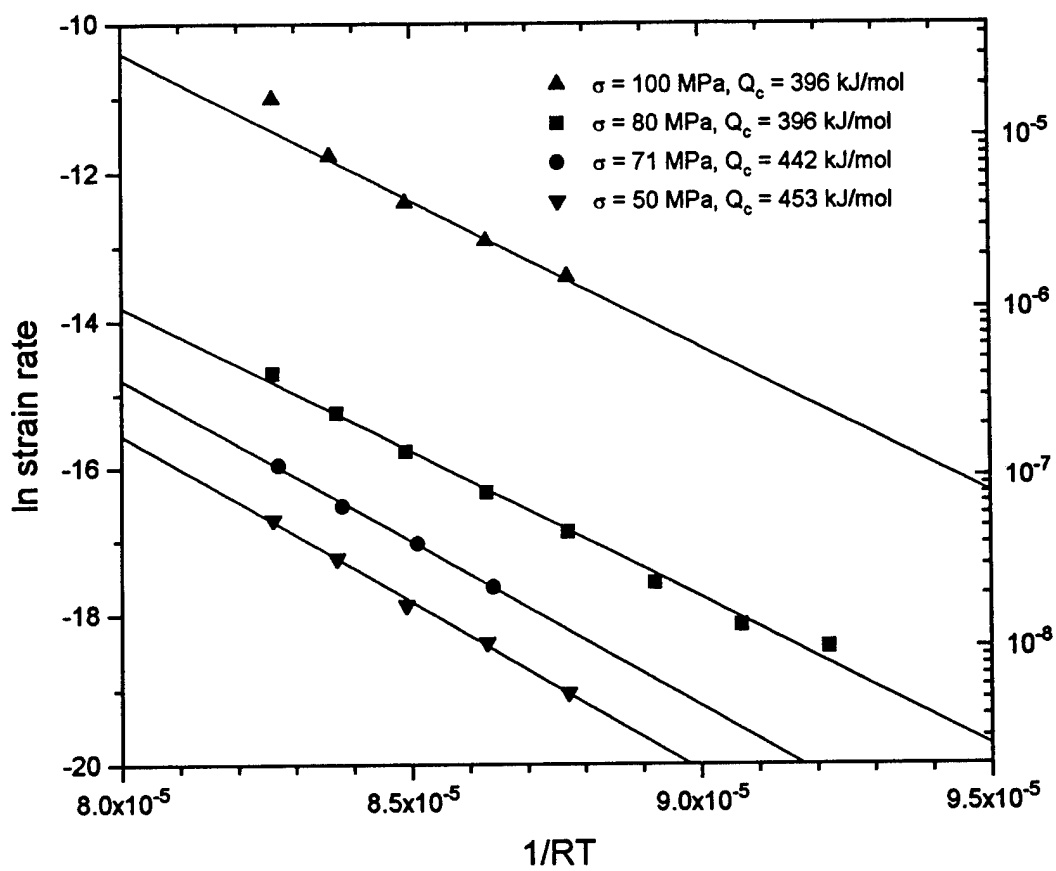
Figure 7. Activation Energy for Creep of Nb-1wt%Zr-0.1wt%C
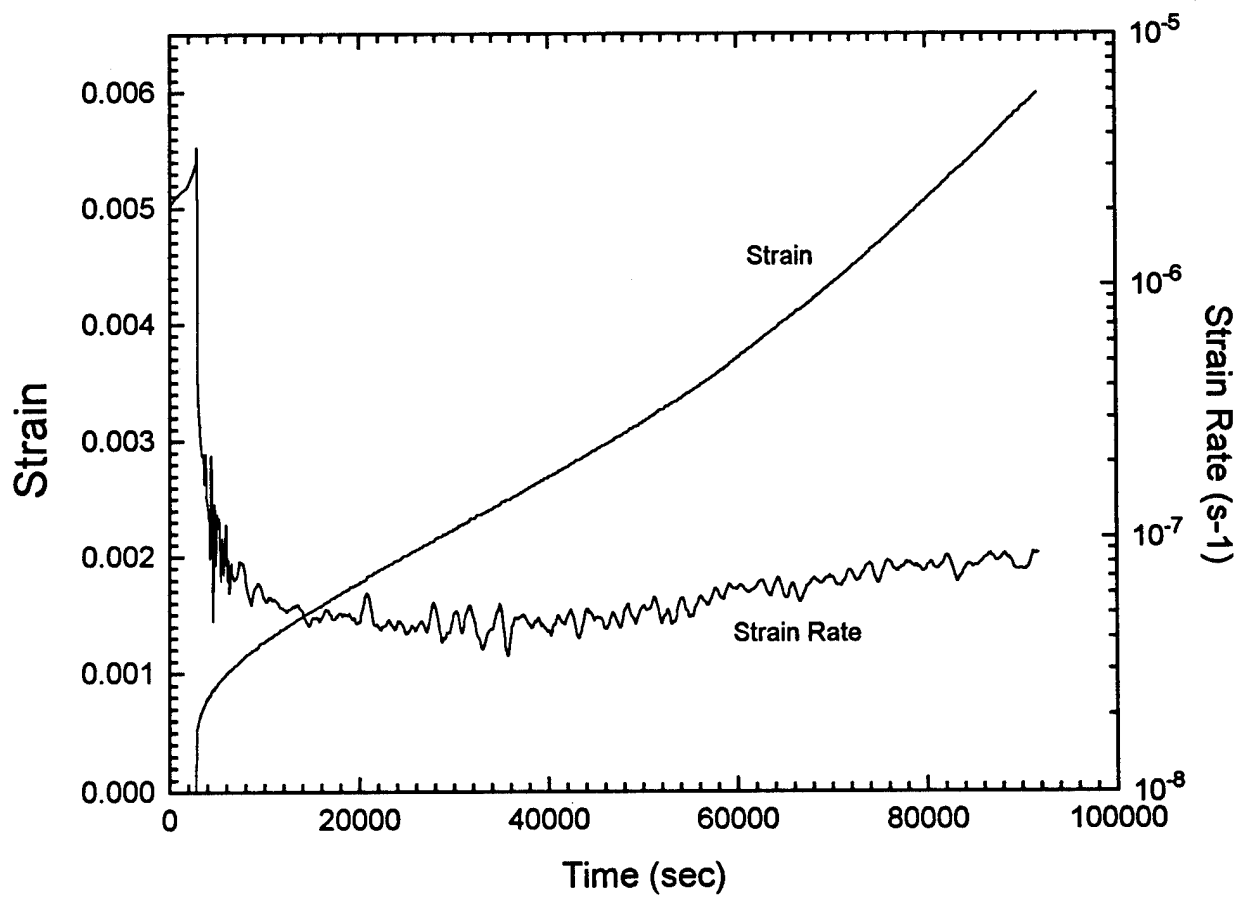
Figure 8. Example of monotonic creep test at 1400 K, 63 MPa illustrating increased strain rate due to particle growth.

MEAN of DISTRIBUTIONS

r	0.10121	μm
r^2	0.01272	μm
r^3	0.00186	μm
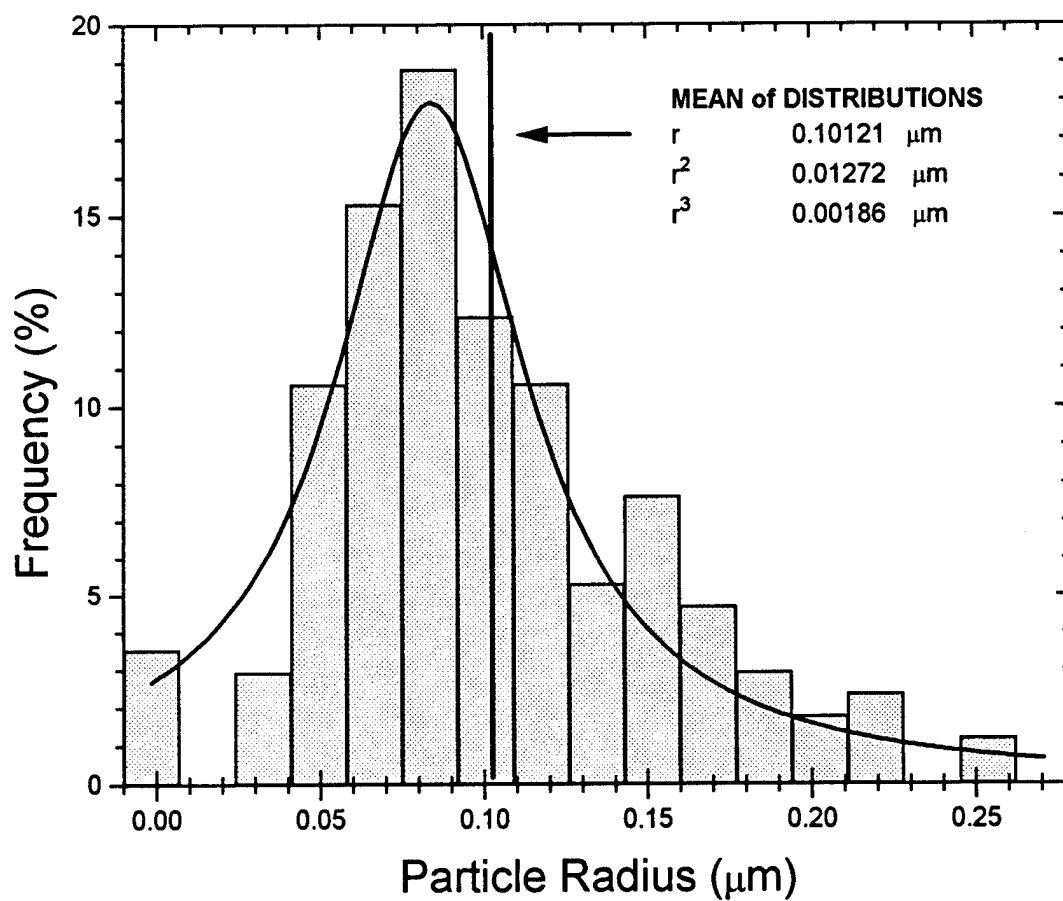
Figure 9. Particle size distribution for carbide particles extracted from alloy crept at 1400 K for 60 hrs.
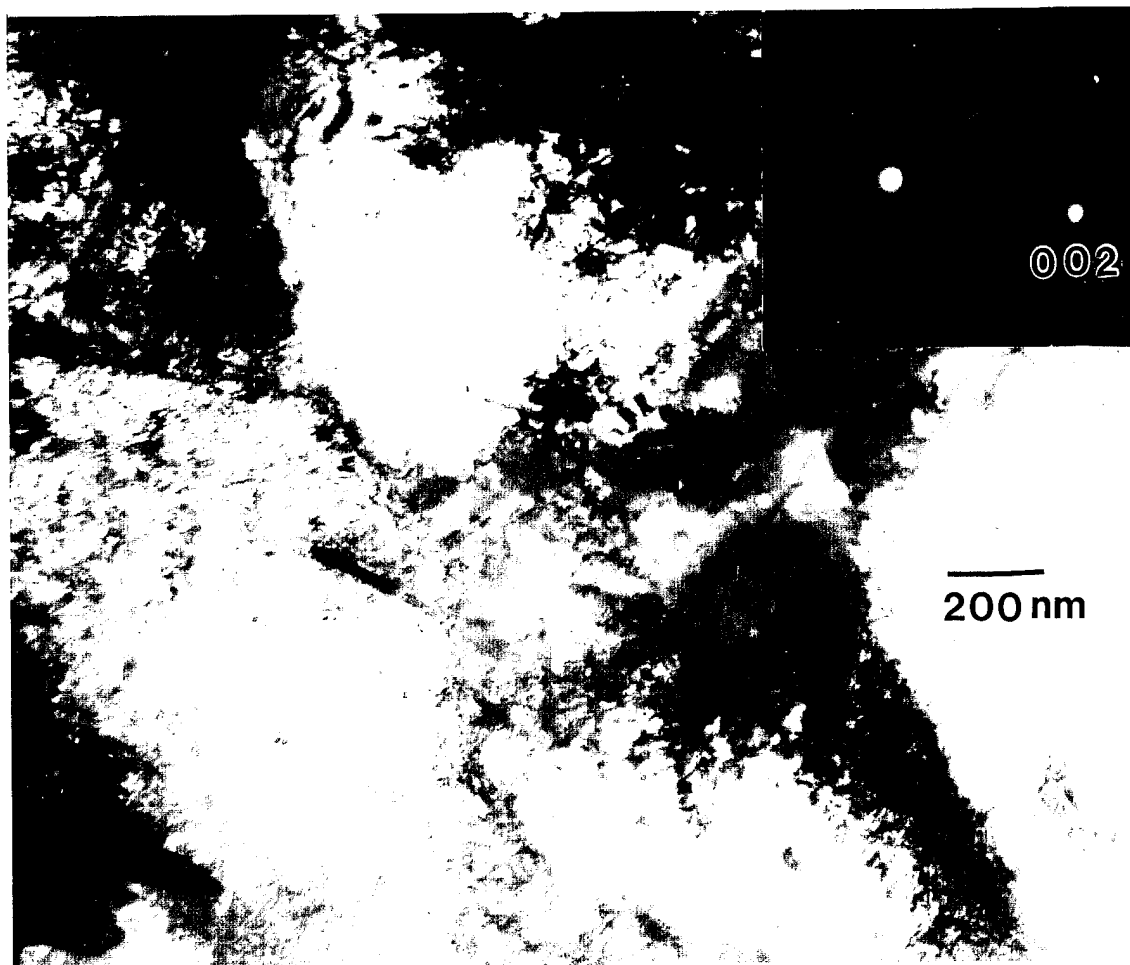
Figure 10a. TEM micrograph of Nb-1wt%Zr-0.1wt%C crept to 0.2 strain at 93 MPa and 1300 K. General arrangement of cellular substructure is evident. Cell dimensions range from 0.5 to 1.5 microns. Magnification 46 kX.
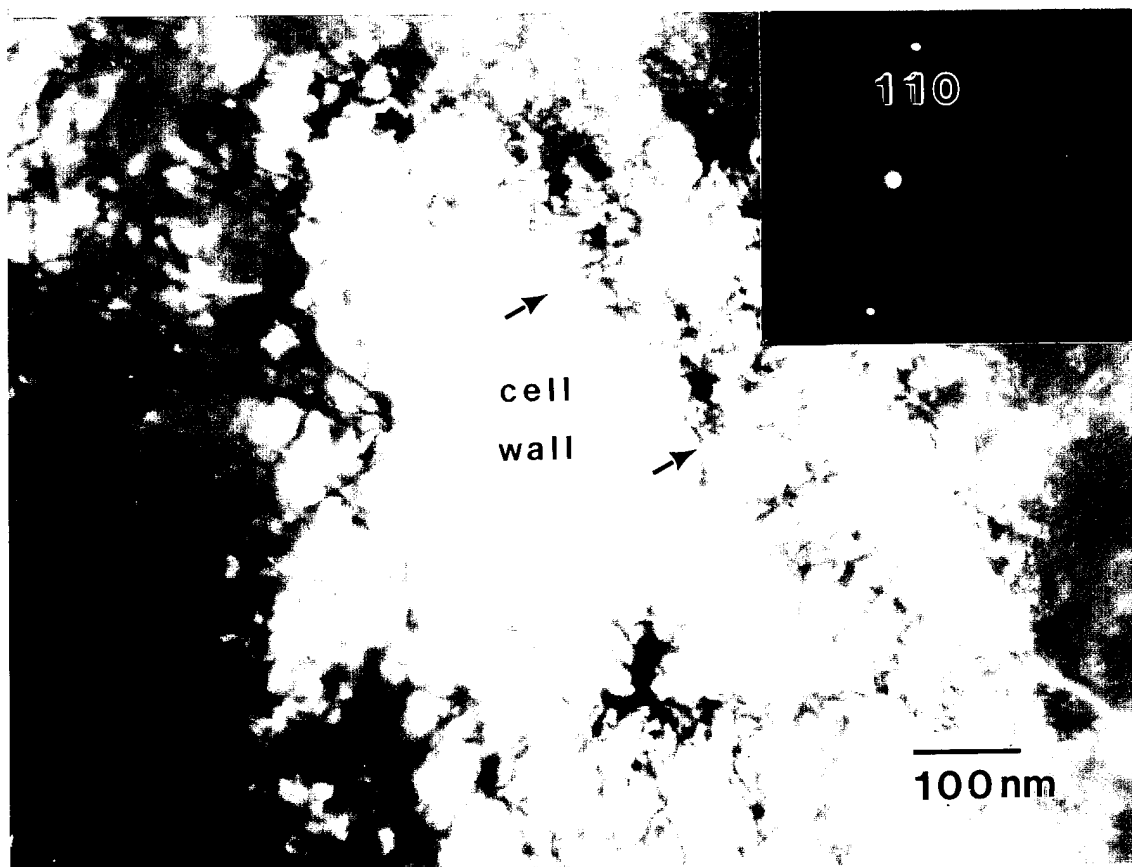
Figure 10b. TEM micrograph of Nb-1wt%Zr-0.1wt%C crept to 0.2 strain at 93 MPa
and 1300 K showing detail of cell wall. Magnification 100 kX.
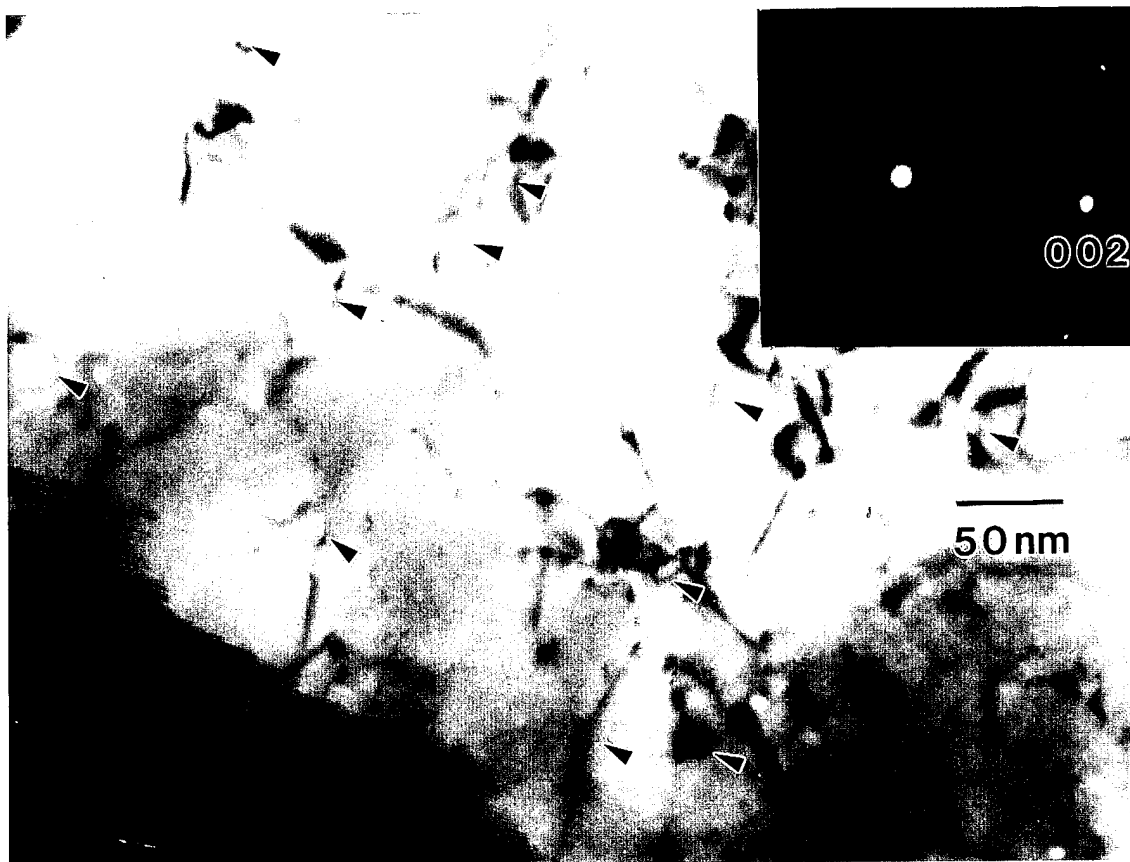
Figure 10c. TEM micrograph of Nb-1wt%Zr-0.1wt%C crept to 0.2 strain at 93 MPa and 1300 K showing detail of cell interior. Relatively few dislocations are present. Carbide particles shown at markers. Magnification 165 kX.
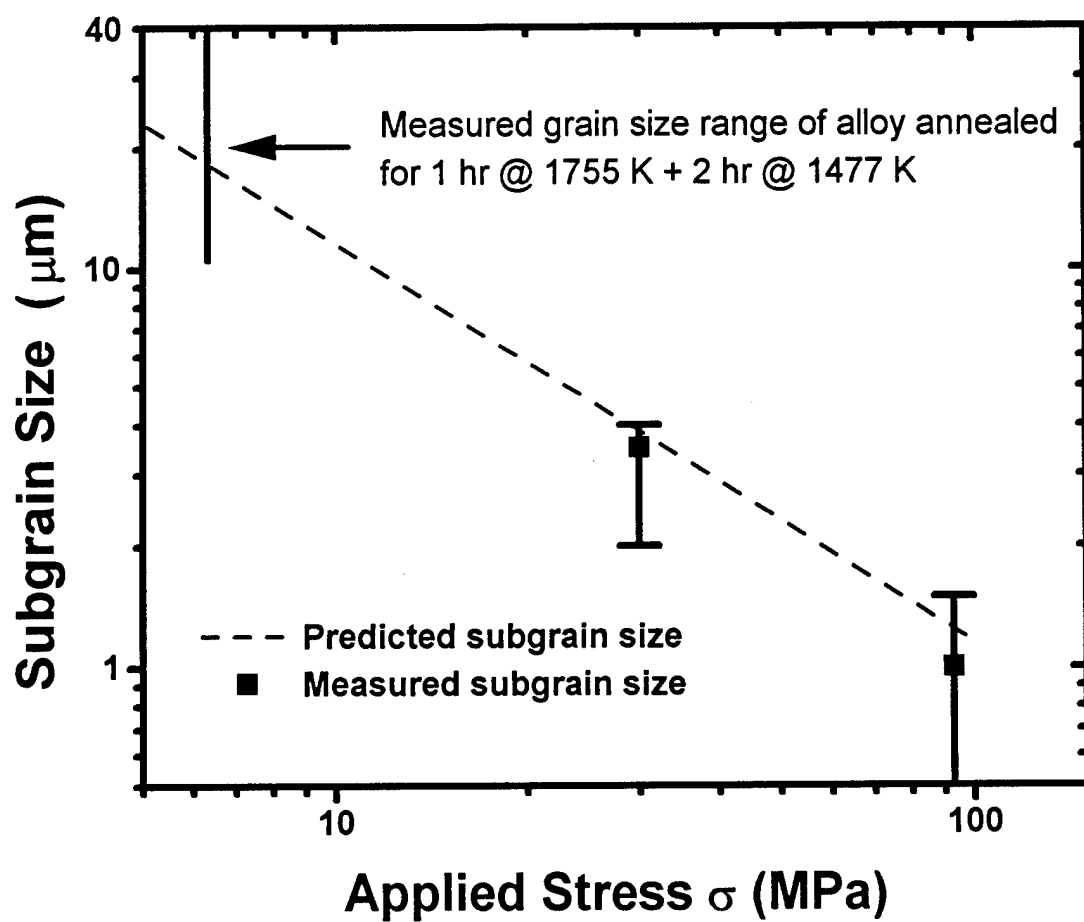
Figure 11. Comparison of measured subgrain size versus applied stress with predicted for Nb-1wt% Zr-0.1wt% C
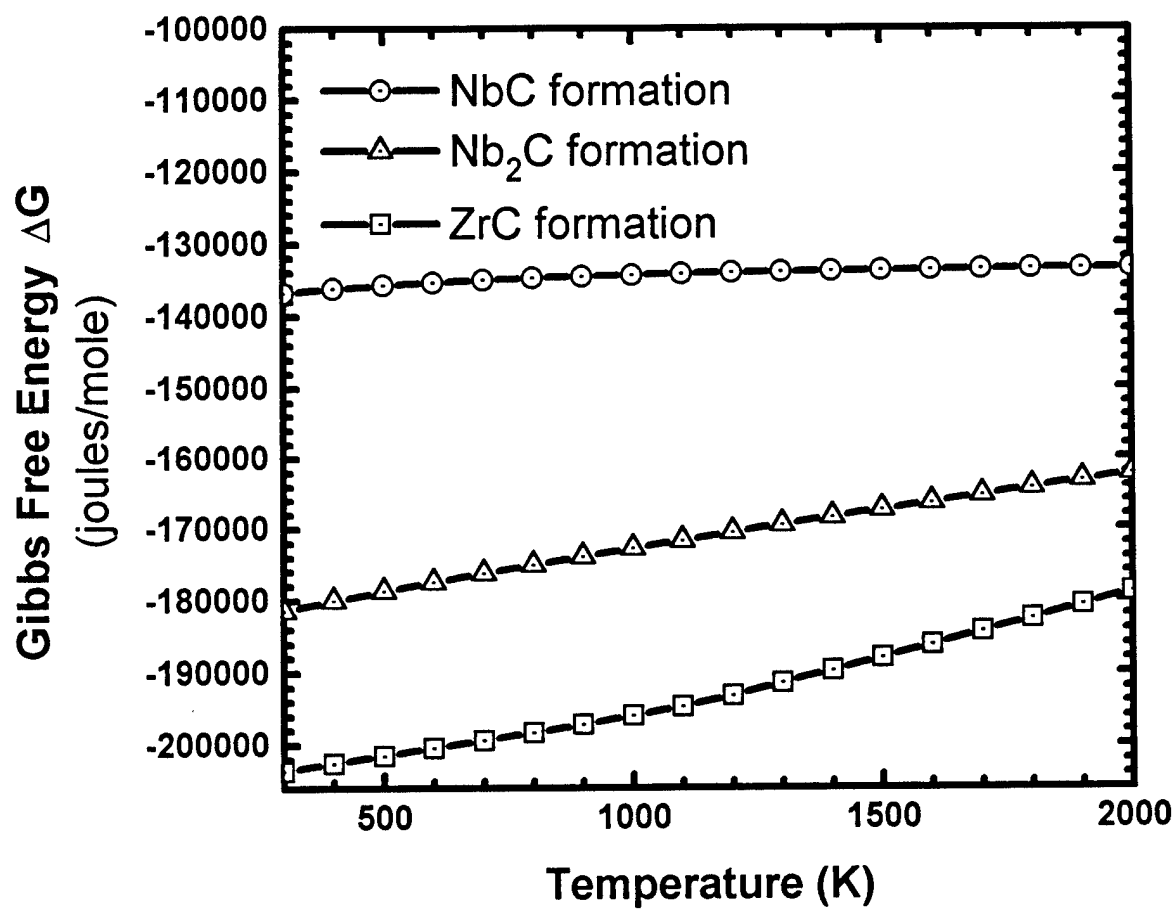
Figure 12. Standard Gibbs free energy versus temperature for carbide formation reactions involving pure components.
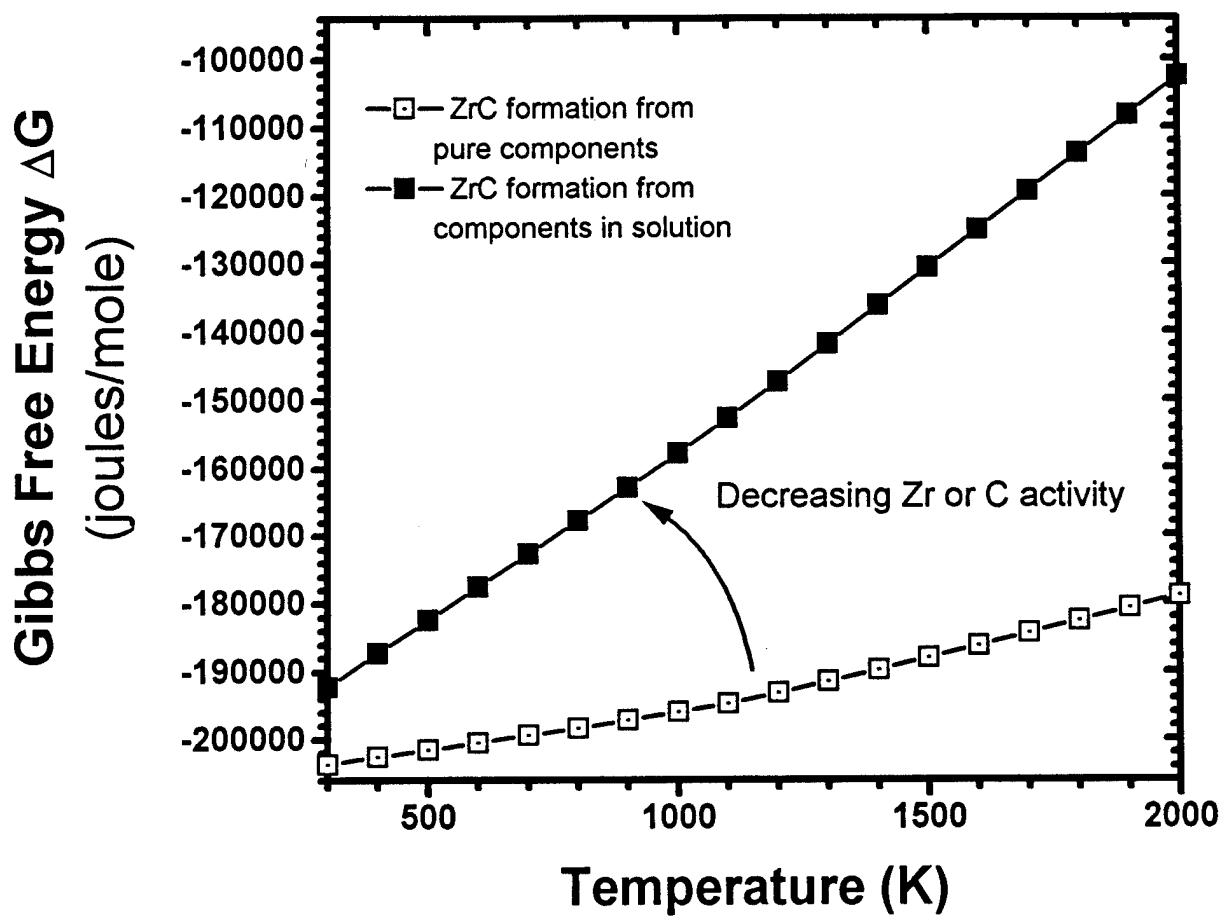
Figure 13. Free energy of formation for ZrC. Free energy
          is altered by the amount RTlnQ and has the effect
          of rotating the free energy line as shown.
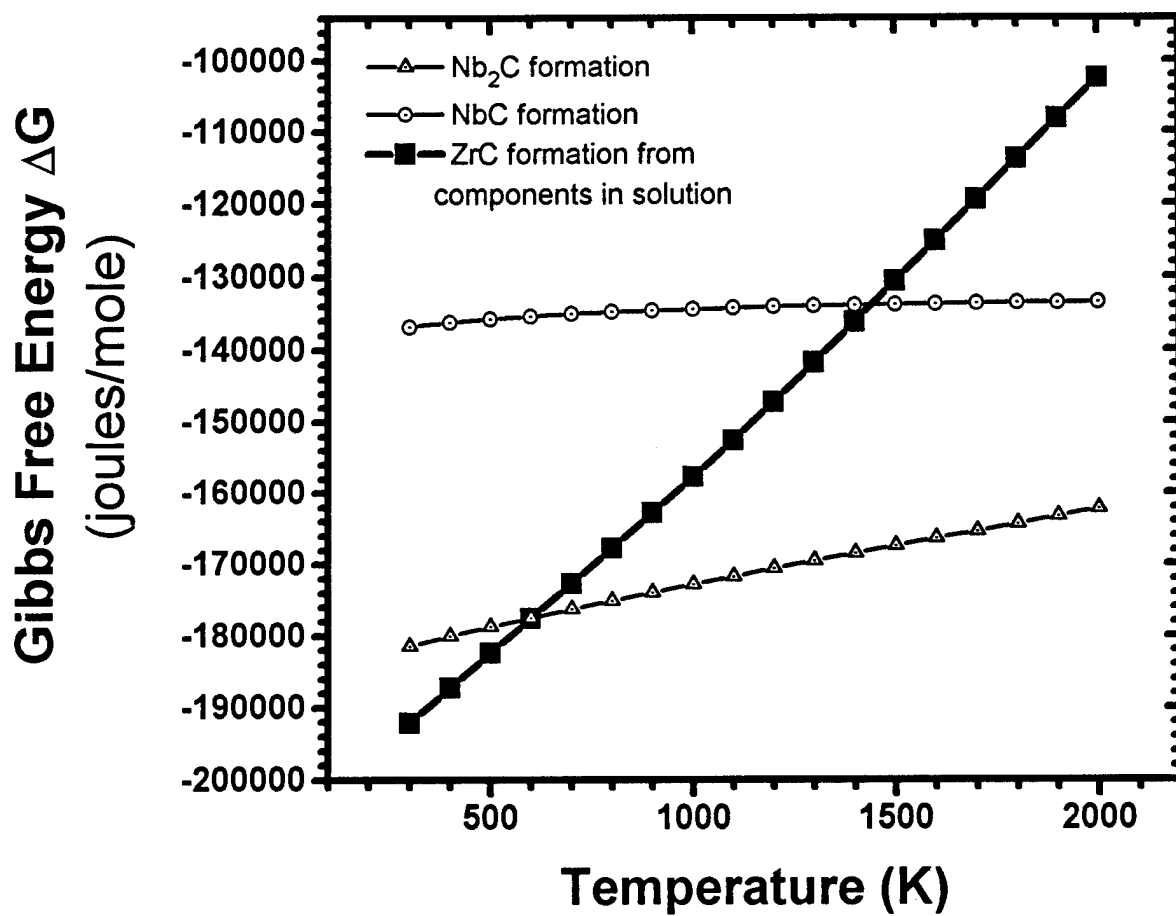
Figure 14. Free energy of formation for NbC, Nb_2C and ZrC when activity of Zr is low as during initial solution treatment.
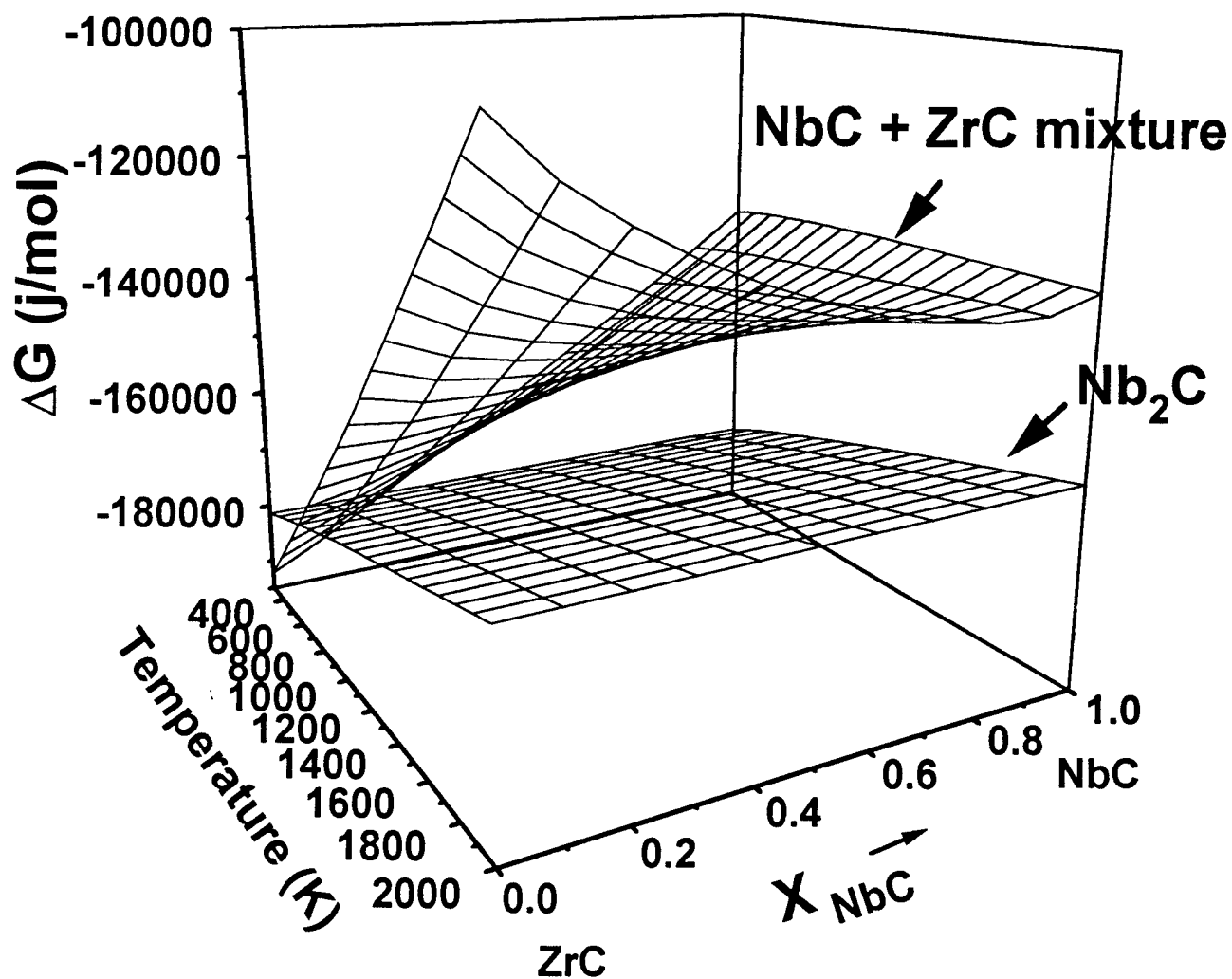
Figure 15. Free Energy surfaces of Nb_2C and (NbC + ZrC) mixture
(for various NbC concentrations) when Zr activity = 0.01
as during initial solution treatment.
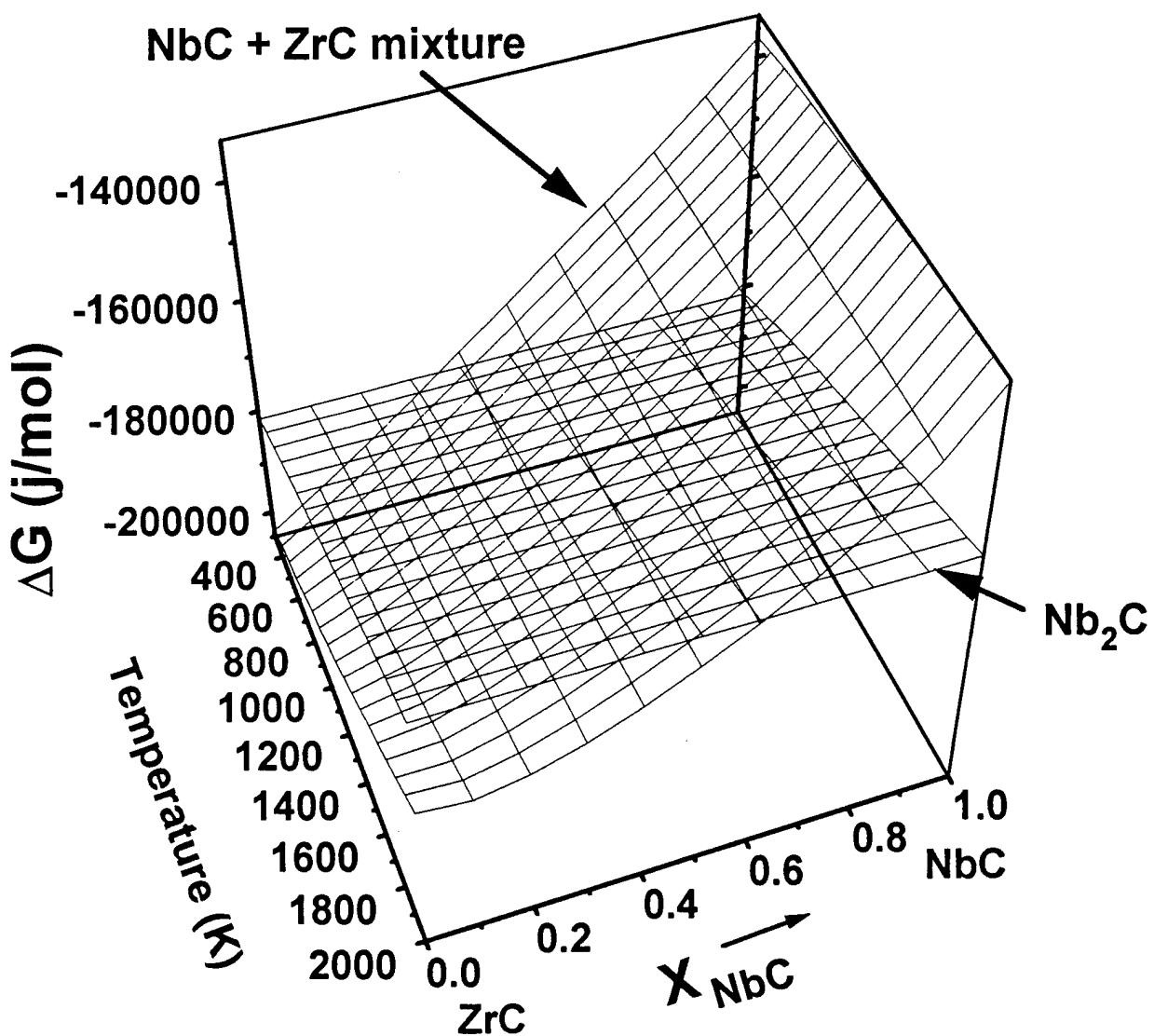
Figure 16. Free energy surfaces of Nb_2C and (NbC + ZrC) mixture when Zr activity = 1. Intersection of two surfaces specifies equilibrium ZrC (and NbC) concentration of mixture.
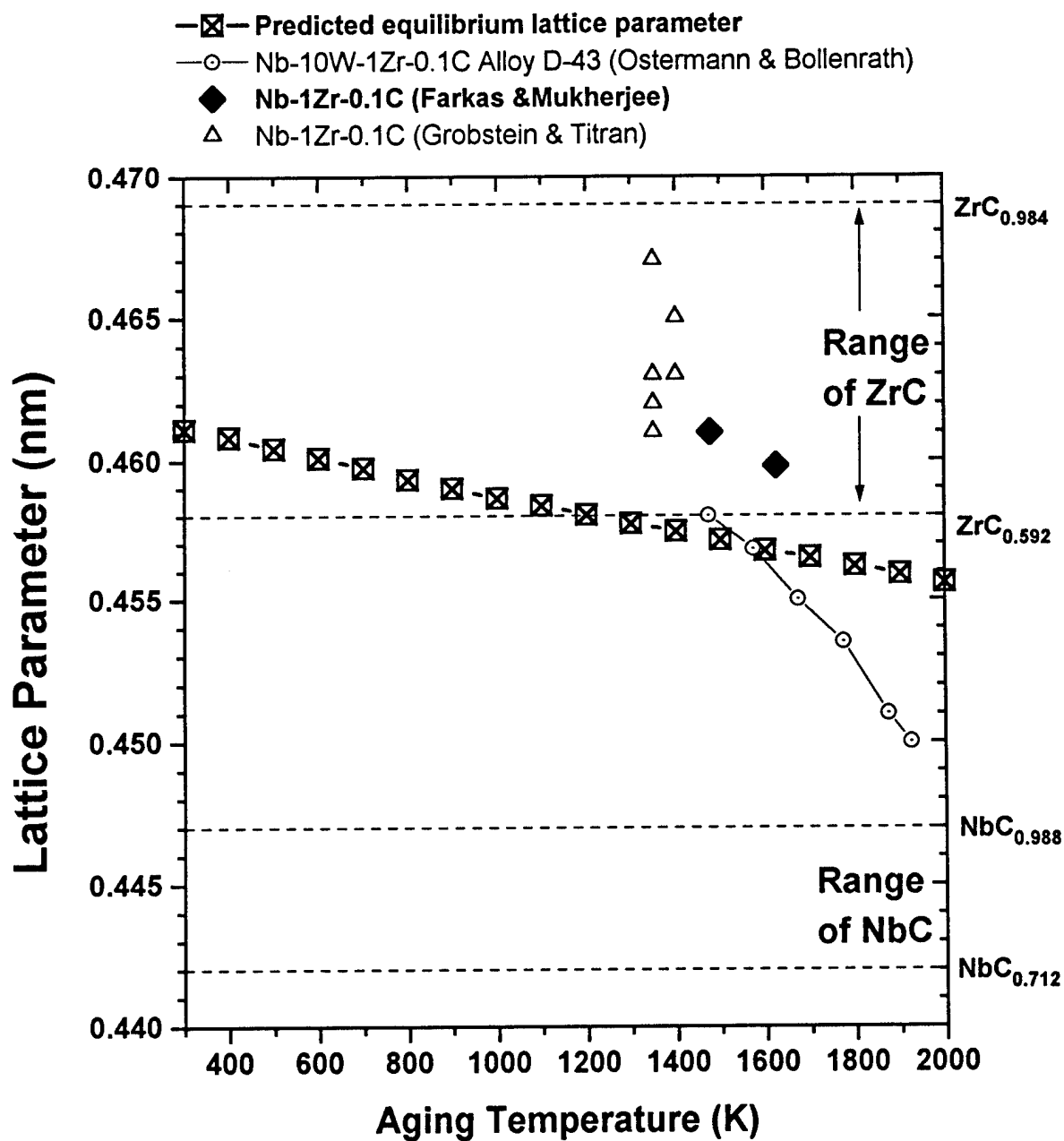
Figure 17. Predicted lattice parameter of NbC + ZrC mixture at equilibrium compared to measured lattice parameters of carbide particles from various alloys at different aging temperatures.

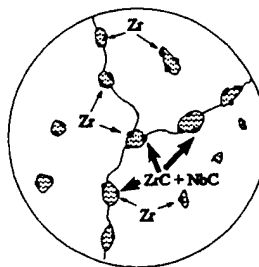Solution treat, alloy constituents
all in solid solution.
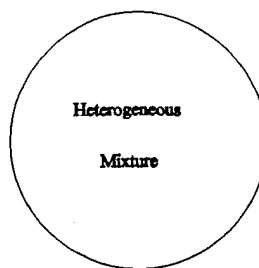
Cool

Heterogeneous formation of Nb_2C
All carbon not taken up in Nb_2C is now
supersaturated; $a_C = 1$
Zirconium remains in solution; $a_{Zr} = X_{Zr}$
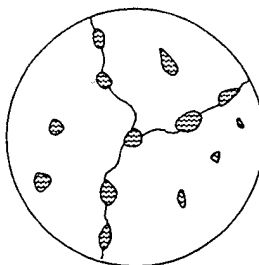
Heat

Zirconium migrates toward Nb_2C particles
raising local concentration and a_{Zr}.
Zr reacts to form NbC+ZrC monocarbide.

Age

Nb_2C is consumed in transformation (shrinks
or dissolves). Mixed carbide which forms is
more evenly distributed in matrix.

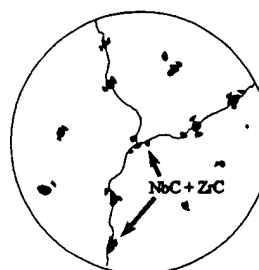Figure 18. Model of transformation of Nb_2C to mixed monocarbide form.